Author/s:
Janetzki, JT;Chegerev, MG;Gransbury, GK;Gable, RW;Clegg, JK;Mulder, RJ;Jameson, GNL;Starikova, AA;Boskovic, C

Title:
Controlling Spin Crossover in a Family of Dinuclear Fe(III) Complexes via the Bis(catecholate) Bridging Ligand

Date:
2023-09-25

Citation:
Janetzki, J. T., Chegerev, M. G., Gransbury, G. K., Gable, R. W., Clegg, J. K., Mulder, R. J., Jameson, G. N. L., Starikova, A. A. & Boskovic, C. (2023). Controlling Spin Crossover in a Family of Dinuclear Fe(III) Complexes via the Bis(catecholate) Bridging Ligand. Inorganic Chemistry, 62 (38), pp.15719-15735. https://doi.org/10.1021/acs.inorgchem.3c02598.

Controlling Spin Crossover in a Family of Dinuclear Fe(III) Complexes via the Bis(catecholate) Bridging Ligand

Jett T. Janetzki,[1] Maxim Chegerev,[2] Gemma K. Gransbury,[3] Robert W. Gable,[1] Jack K. Clegg,[2] Roger J. Mulder,[4] Guy N. L. Jameson, [1] Alyona A. Starikova[2] and Colette Boskovic[1]*

[1] School of Chemistry, University of Melbourne, Victoria 3010, Australia

[2] Institute of Physical and Organic Chemistry, Southern Federal University, 344090, Rostov-on-Don, Russian Federation

[3] Department of Chemistry, The University of Manchester, Manchester, M13 9PL,United Kingdom

[4] School of Chemistry and Molecular Biosciences, University of Queensland, St Lucia, Queensland 4072, Australia

[5] CSIRO Manufacturing, Clayton, Victoria 3168, Australia

* c.boskovic@unimelb.edu.au

ABSTRACT

Spin crossover (SCO) complexes can reversibly switch between low spin (LS) and high spin (HS) states, affording possible applications in sensing, displays and molecular electronics. Dinuclear SCO complexes with access to [LS-LS], [LS-HS] and [HS-HS] states may offer increased levels of functionality. The nature of the SCO interconversion in dinuclear complexes is influenced by the local electronic environment. We report the synthesis and characterization of [{Fe^{III}(tpa)}$_2$spiro]$(PF_6)_2$ (**1**), [{Fe^{III}(tpa)}$_2$$Br_4$spiro]$(PF_6)_2$ (**2**) and [{Fe^{III}(tpa)}$_2$thea]$(PF_6)_2$ (**3**) (tpa = tris(2-pyridylmethyl)amine, spiroH_4 = 3,3,3′,3′-tetramethyl-1,1′-spirobi(indan)-5,5′,6,6′-tetraol, Br_4spiroH_4 = 3,3,3′,3′-tetramethyl-1,1′-spirobi(indan)-4,4′,7,7′-tetrabromo-5,5′,6,6′-tetraol, theaH_4 = 2,3,6,7-tetrahydroxy-9,10-dimethyl-9,10-dihydro-9,10-ethanoanthracene), utilizing non-conjugated bis(catecholate) bridging ligands. In the solid state, magnetic and structural analysis shows **1** remains in the [HS-HS] state, while **2** and **3** undergo a partial SCO interconversion upon cooling from room temperature involving the mixed [LS-HS] state. In solution, all complexes undergo SCO from [HS-HS] at room temperature, via [LS-HS] to mixtures including [LS-LS] at 77 K, with the extent of SCO increasing in the order **1** < **2** < **3**. Gas phase density functional theory (DFT) calculations suggests a [LS-LS] ground state for all complexes, with the [LS-HS] and [HS-HS] states successively destabilized. The relative energy separations indicate ligand field strength increases following spiro^{4-} < Br_4spiro^{4-} < thea^{4-}, consistent with solid state magnetic behavior. All three complexes show stabilization of the [LS-HS] state in relation to the midpoint energy between [LS-LS] and [HS-HS]. The relative stability of the [LS-HS] state increases with increasing ligand field strength of the bis(catecholate) bridging ligand, in the order **1** < **2** < **3**. The bromo substituents of Br_4spiro^{4-} increase the ligand field strength relative to spiro^{4-}, while the stronger ligand field provided by thea^{4-} arises from extension of the overlapping π-orbital system

across the two catecholate units. This study highlights how SCO behavior in dinuclear complexes can be modulated by the bridging ligand, providing useful insights for the design of molecules that can be interconverted between more than two states.

INTRODUCTION

Spin crossover (SCO) involves a stimulated reversible interconversion between low spin (LS) and high spin (HS) states in transition metal complexes with d^4 – d^7 electronic configurations.[1] This phenomenon is possible in the presence of a suitable ligand field and is typically induced with temperature, pressure or light irradiation.[2] The change in the magnetic, optical, structural and electronic properties of SCO compounds is relevant for possible applications in sensors, displays, spintronics and molecular electronics.[3–6] The most common metal ion to display SCO is Fe(II),[7–9] and significant advances have been made in the practical deployment of Fe(II) SCO complexes.[6,10–14] Iron(III) spin crossover compounds,[15] though relatively less explored than Fe(II), have seen use in molecular junctions,[16] forming nanowires[17] and self-assembled materials,[18] and have shown interesting hysteretic and light-induced properties.[19] Typically an N_4O_2 coordination sphere gives rise to Fe(III) SCO.[15,19,20] The continual development of SCO complexes based on ions other than Fe(II) is important to continually expand functionality and properties.

Discrete dinuclear SCO complexes have garnered interest, including for their ability in some cases to access three possible spin states: [LS-LS], [LS-HS], and [HS-HS]. An accessible [LS-HS] state can potentially afford two-step SCO,[21–23] opening possibilities for ternary data storage and more complex logic processing in molecular electronics and spintronics.[24] It can also allow investigation of the impact of intramolecular electronic and magnetic interactions on SCO.[7,25] The origin of two-step SCO for dinuclear Fe(II) complexes versus one concerted interconversion was initially thought to arise from intramolecular cooperativity between binding pockets.[21,22,26,27] However, the current understanding is that the structural changes upon SCO at one Fe(II) site do not play a major role in inducing SCO at a second site, even with tightly constrained ligands.[28,29] Instead, the nature of the SCO is dictated by the local electronic structure

at each of the Fe(II) centers.[29] For example, in the specific Fe(II) complexes studied by Cirera and Ruiz, decreasing the ligand field stabilized the [LS-HS] state and favored a two-step interconversion.[29] Unlike for Fe(II),[7] dinuclear Fe(III) SCO compounds showing two-step SCO are far rarer,[23,30–32] and so have been relatively less studied. As such, understanding the factors that govern two-step SCO in Fe(III) complexes has not been explored, hindering rational design.

Within Fe(III) SCO research, Fe(III)-catecholate (cat^{2-}) complexes, originally used to study diol cleavage, can undergo thermally-induced SCO.[20,33,34] A number of these Fe(III)-cat SCO complexes, in which $[Fe^{III}(tpa)(cat)]^{+}$ (tpa = tris(2-pyridylmethyl)amine) is the prototypical example,[20] have been studied with varying substituents on the catecholate and N-donor ligands.[33–39] Increasing the electron-withdrawing nature of the N-donor ligand stabilizes the LS state.[39,40] Interestingly, the ground state for this family of complexes incorporates Fe(II)-SQ ($SQ^{\bullet-}$ = semiquinonate), giving rise to mixing of Fe(III)-cat and Fe(II)-SQ electronic states.[35,38,41] Electron donating substituents on the catecholate ligand increase the accessibility of the Fe(II)-SQ state.[38,39,42] This ability to access Fe(II)-SQ suggested possibility of Fe(III)-cat ⇌ Fe(II)-SQ valence tautomerism (VT) for these complexes instead of, or in addition to, SCO. Indeed, some of us have recently reported the complex $[Fe^{III}(tpa)(3,6\text{-dbcat})]X$ (3,6-dbcat = 3,6-di-*tert*-butylcatechol), which shows SCO for X = PF_6^-, BPh_4^- and ClO_4^-, whilst VT with X = BF_4^-.[43]

Considering the important role played by the bis(dioxolene) bridging ligand in mediating valence tautomerism in dinuclear cobalt complexes,[24,44] we sought to investigate the situation for related dinuclear Fe(III) complexes. The focus herein is to explore the role of the bridging ligand in influencing the nature of the SCO transition in dinuclear Fe(III) complexes in order to understand how two-step Fe(III) SCO could be achieved. Considering that Fe(III)-catecholate compounds can show SCO, $\{Fe^{III}(tpa)\}^{3+}$ units bridged by bis(dioxolene) ligands could potentially

display two-step SCO. Numerous bis(dioxolene) ligands are available,[24] with examples of bis(dioxolene)-bridged dinuclear complexes studied in the literature including $[\{Co(Me_ntpa)\}_2L]^{2+}$ and $[\{Pt(X)\}_2thea]$ (Me_ntpa = tris(2-pyridylmethyl)amine, n = 0−3 is degree of methylation at 6-position on pyridine ring); L = 3,3,3′,3′- tetramethyl-1,1′-spirobi(indan)-5,5′,6,6′-tetraol, 3,3,3′,3′-tetramethyl-1,1′-spirobi(indan)-4,4′,7,7′-tetrabromo-5,5′,6,6′-tetraol, 6,6′-((1,4-phenylenebis-(methylene))bis(sulfanediyl))bis(3,5-di-tert-butyl-benzene- 1,2-diol); $theaH_4$ = and 2,3,6,7-tetrahydroxy-9,10-dimethyl-9,10-dihydro-9,10-ethanoanthracene; X = 4,4′-bis(tert-butyl)-2,2′-bipyridyl, 1,2-bis(diphenylphosphino)benzene, 1,2-bis(diphenylphosphino)ethane).[24,44,45] The variety of bis(dioxolene) ligands available allows for the synthesis of an easily modified family of compounds that can study how varying the redox-potentials, electronic communication strength and conjugation impacts SCO behavior, as well as possible VT, magnetic coupling, and electronic structure.

We report the use of the non-conjugated bis(catecholate) ligands 3,3,3′,3′- tetramethyl-1,1′-spirobi(indan)-5,5′,6,6′-tetraol ($spiroH_4$), 3,3,3′,3′-tetramethyl-1,1′-spirobi(indan)-4,4′,7,7′-tetrabromo-5,5′,6,6′-tetraol ($Br_4spiroH_4$), and 2,3,6,7-tetrahydroxy-9,10-dimethyl-9,10-dihydro-9,10-ethanoanthracene ($theaH_4$) to bridge $\{Fe^{III}(tpa)\}^{3+}$ moieties to give compounds $[\{Fe^{III}(tpa)\}_2spiro](PF_6)_2$ (**1**), $[\{Fe^{III}(tpa)\}_2Br_4spiro](PF_6)_2$ (**2**), and $[\{Fe^{III}(tpa)\}_2thea](PF_6)_2$ (**3**) (Scheme 1). The bis(catecholate) ligands were chosen to study how the difference in ligand field and electronic communication strength affects the SCO behavior. Through a combination of structural, magnetic, spectroscopic, electrochemical and computational analysis, we have discovered how the bis(catecholate) ligands influence the SCO behavior and the potential propensity toward two-step SCO.

Scheme 1. Dinuclear Fe(III) metal complexes $[\{Fe^{III}(tpa)\}_2spiro](PF_6)_2$ (**1**), $[\{Fe^{III}(tpa)\}_2Br_4spiro](PF_6)_2$ (**2**), and $[\{Fe^{III}(tpa)\}_2thea](PF_6)_2$ (**3**) studied in this work, with numbering scheme. All complexes are isolated as the PF_6^- salt.

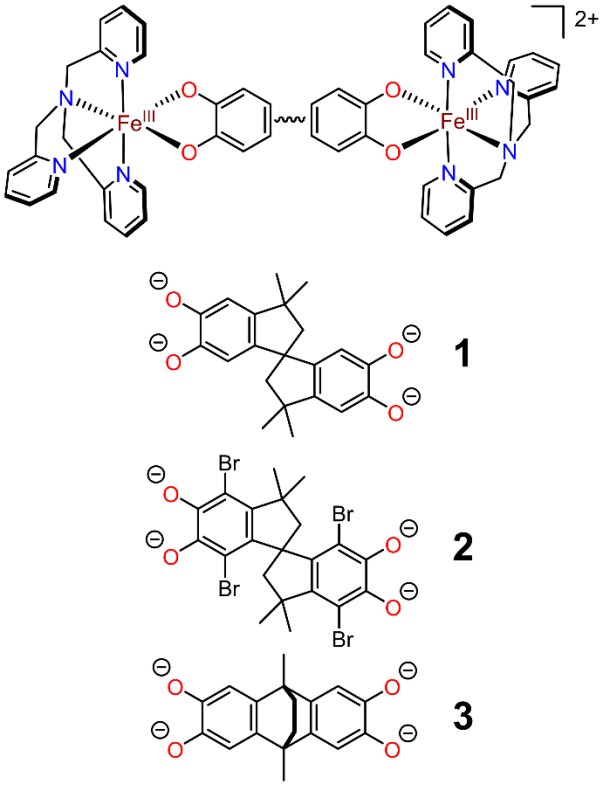

RESULTS AND DISCUSSION

Synthesis

The dinuclear compounds **1**, **2** and **3** were prepared under an atmosphere of N_2 in methanol (MeOH) by first combining the anhydrous $FeCl_3$ salt with tpa (tris(2-pyridylmethyl)amine) to form the $[Fe^{III}(tpa)Cl_2]^+$ intermediate, before combining with the appropriate bis(catecholate) ligand (**1**, spiroH_4; **2**, Br$_4$spiroH_4, **3**, theaH_4) deprotonated with Et_3N. This produced a purple (**1**), blue (**2**), or

violet (**3**) solution. After addition of the PF_6^- anion and 24 hours at −18 °C, darkly colored blue or purple microcrystals formed. In solution, the compounds rapidly reacted with O_2 when exposed to air, turning brown. In the solid-state, decomposition occurs over weeks if stored in air. Recrystallisation of the three compounds by layering a highly saturated acetonitrile (MeCN) solution with diisopropylether (*i*Pr_2O) under N_2 resulted in single crystals for **2** and **3**, and microcrystalline solid for **1**. Unsuccessful attempts were made to grow larger crystals of **1** with a range of solvent combinations. Upon collection and air drying, bulk samples of **2** lose *i*Pr_2O and absorb water to yield **2**·1.3H_2O, while **1** and **3** absorb water to give **1**·2H_2O·0.5*i*Pr_2O and **3**·2H_2O·0.5*i*Pr_2O. The purity and solvation of **1**·2H_2O·0.5*i*Pr_2O, **2**·1.3H_2O, and **3**·2H_2O·0.5*i*Pr_2O were confirmed by elemental analysis (EA) and thermogravimetric analysis (TGA) (Figure S1). Powder X-ray diffraction (PXRD) showed that bulk samples of **2**·1.3H_2O and **3**·2H_2O·0.5*i*Pr_2O are phase pure (Figure S2). The PXRD pattern for compound **1**·2H_2O·0.5*i*Pr_2O differs from **2**·1.3H_2O (Figure S2), despite the same crystallization method and relatively similar molecular structure, indicating different crystal packing.

Structure Description

The solid-state structure of **2**·*i*Pr_2O·*x*H_2O (*x* = 0, 1) was determined by single crystal X-ray diffraction at 30, 100, 150, 250, 300 and 350 K (Figure 1, Table S1, S2). Compound **2**·*i*Pr_2O·*x*H_2O crystallizes as dark blue irregular blocks in the orthorhombic space group *Pbcn*, with half a molecule of $[\{Fe^{III}(tpa)\}_2Br_4spiro]^{2+}$ and one PF_6^- in the asymmetric unit. For the 30 and 100 K structures, the PF_6^- anion is ordered, while at all other temperatures it is disordered over two positions. For the 30 K structure, an ordered *i*Pr_2O was located and modelled. For 100 – 350 K, the *i*Pr_2O is disordered due to the higher temperature. A solvent mask regime was used to model the disordered solvent and, based on the residual volume and electron count in conjunction with

elemental analysis, was assigned to one iPr$_2$O and one H$_2$O per formula unit for 100-300 K, and one iPr$_2$O for 350 K. The presence of counterions and solvent in the crystal structure are consistent with the formula **2**·iPr$_2$O·xH$_2$O (x = 0, (30, 350 K), 1 (100, 150, 200, 250, 300 K). The single crystal solvation for **2** differs from the bulk recrystallized compound, with loss of iPr$_2$O upon collection and absorption of H$_2$O, as previously observed for the cobalt analogue.[24] Powder X-ray diffraction (PXRD) collected at 100 K confirmed that the bulk **2**·1.3H$_2$O sample was phase pure and matched with the diffraction pattern calculated from the single-crystal X-ray structure of **2**·iPr$_2$O·xH$_2$O (Figure S2). The structure measured for **2**·iPr$_2$O·xH$_2$O at 100 K was identical following either slow or rapid cooling, discounting possible phase trapping.[46]

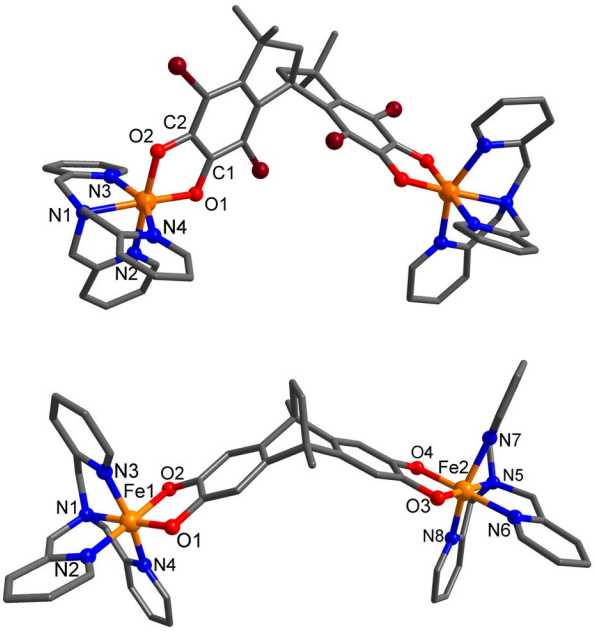

Figure 1. Complex cations in **2**·iPr$_2$O·xH$_2$O (top) and **3**·Et$_2$O (bottom) at 100 K. Hydrogen atoms have been omitted for clarity. Color code: C (dark grey), N (blue), O (red), Br (dark red), Fe (orange).

Each iron center is coordinated by one tpa ligand and the Br_4spiro^{4-} ligand (Figure 1). Due to the inequivalence of the O1 and O2 oxygen atoms of Br_4spiro^{4-}, geometric isomerization is possible; O1 is in closer proximity to the spirocyclic carbon (*proximal*) whilst O2 is further away (*distal*).[24] In **2**, as the *proximal* oxygens are *trans* to the tertiary-amine nitrogen of the tpa, the isomer is *proximal-proximal* (*pp*). To determine the iron oxidation and spin state, we used the Fe−O and Fe−N bond lengths and octahedral distortion parameters (octahedral *SHAPE* index, Σ and Θ).[47–49] The *SHAPE* index calculated by SHAPE 2.1 represents the distortion of the coordination sphere from an ideal polyhedron,[47,48] and the Σ and Θ parameters calculated using OctaDist represent the angles of distortion in an octahedron.[49] In the equivalent mononuclear Fe(III) analogues with tpa and substituted catecholate ligands, LS-Fe(III) typically has Fe−N and Fe−O bond lengths of 1.95-2.09 and 1.88-1.90 Å, respectively, whereas HS-Fe(III) has longer Fe−N and Fe−O bond lengths of 2.09-2.15 and 1.91-1.93 Å, respectively.[34,37,41,50] The bond lengths of HS-Fe(II) complexes with N_4O_2 coordination spheres are typically longer than HS-Fe(III), with Fe−N and Fe−O bond lengths of 2.18-2.25 and 2.05-2.12 Å respectively.[51,52] Typically, the HS-Fe(III) state has larger degrees of distortion of the octahedral coordination environment compared to LS-Fe(III).[37] At 350 K, the average Fe−N and Fe−O bond lengths for **2**·*i*Pr_2O·*x*H_2O of 2.160(3) and 1.928(2) Å, respectively, octahedral *SHAPE* of 1.925, and Σ and Θ of 103 and 299 respectively (Table 1), indicate both iron centers are HS-Fe(III).

Table 1. Selected Interatomic Distances (Å) and Distortion Parameters for **2**·iPr$_2$O·xH$_2$O.

	30 K	**100 K**	**150 K**	**200 K**	**250 K**	**300 K**	**350 K**
Interatomic Distances							
Fe−O_1	1.902(3)	1.910(2)	1.914(2)	1.915(2)	1.914(2)	1.916(2)	1.913(2)
Fe−O_2	1.925(3)	1.933(2)	1.935(2)	1.937(2)	1.942(2)	1.942(2)	1.944(2)
Fe−N_1	2.144(4)	2.166(2)	2.175(2)	2.181(2)	2.185(2)	2.186(2)	2.192(3)
Fe−N_2	2.081(4)	2.106(2)	2.114(2)	2.123(2)	2.126(2)	2.127(2)	2.137(3)
Fe−N_3	2.117(4)	2.140(2)	2.144(2)	2.148(2)	2.148(2)	2.156(2)	2.149(3)
Fe−N_4	2.119(5)	2.135(2)	2.147(2)	2.153(2)	2.156(2)	2.163(3)	2.164(3)
C_1−O_1	1.329(5)	1.335(3)	1.335(3)	1.333(3)	1.334(3)	1.336(3)	1.333(3)
C_2−O_2	1.333(5)	1.331(3)	1.332(2)	1.335(3)	1.335(3)	1.331(3)	1.333(3)
Fe···Fe	10.416(1)	10.416(2)	10.423(2)	10.424(2)	10.424(2)	10.427(2)	10.448(2)
Distortion Parameters							
SHAPE (O_h)[a]	1.577	1.753	1.802	1.849	1.867	1.925	1.925
Σ/° [b]	91.6	96.4	98.5	100.1	100.9	102.1	102.9
Θ/° [b]	267.2	284.2	289.0	293.0	294.7	295.8	298.6
MOS	−1.70(9)	−1.71(7)	−1.73(7)	−1.74(5)	−1.76(5)	−1.75(6)	−1.75(6)

[a]*SHAPE* index for octahedral geometry in SHAPE 2.1.[47,48] A value of 0 represents a perfect octahedron. [b]∑ = sum of the deviation of the 12 N/O−Co−N/O angles from 90°. Θ = sum of the deviation of 24 unique torsional angles between the N/O atoms on opposite triangular faces of the octahedron from 60°, providing the degree of trigonal distortion from an octahedron to trigonal prism. These were calculated using OctaDist - a program for determining the structural distortion of the octahedral complexes. For a perfect octahedron, ∑ and Θ are zero.[49]

On cooling to 30 K, there is a steady contraction of the Fe−N and Fe−O bond lengths in **2**·iPr$_2$O·xH$_2$O by 0.04 and 0.01 Å, respectively, to give lengths of 2.115(4) and 1.914(3) Å (Figure 2, Figure S3, Table 1). These bond lengths are longer than the expected values for LS-Fe(III), but coupled with the observed decrease in octahedral *SHAPE*, Σ and Θ parameters (Figure S4, Table 1) are consistent with partial SCO for **2**·iPr$_2$O·H$_2$O, far from complete at 30 K. When compared to the bond-length changes, as well as *SHAPE*, Σ and Θ, from HS to LS in [Fe^{III}(tpa)(Cl_4cat)]$^+$ (Cl_4cat = 3,4,5,6-tetrachlorocatecholate) (Figure S5), the SCO transition occurring for **2**·iPr$_2$O·xH$_2$O can be approximated to ~25-30% interconversion from [HS-HS].[37,50]

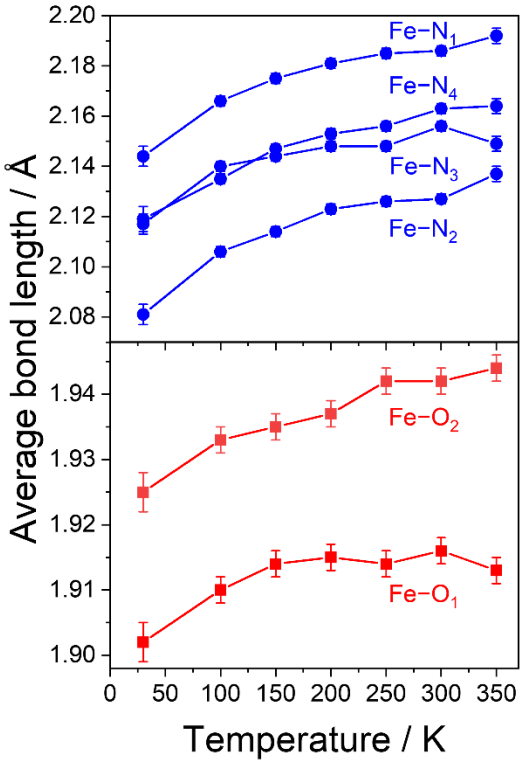

Figure 2. Temperature dependence of the Fe–N (blue) and Fe–O (red) bond lengths for **2**·*i*Pr$_2$O·*x*H$_2$O.

The oxidation state of the Br$_4$spiro^{4-} ligand was quantitatively assigned using the empirical metrical oxidation state (MOS), determined using a least-squared fitting of C–C and C–O bond distances to assign an apparent oxidation state of –2 for a catecholate oxidation state and –1 for a semiquinonate oxidation state.[53,54] The average MOS of the Br$_4$spiro^{4-} in the range 30–350 K is −1.73(6), compared to −2.03(9) to uncoordinated Br$_4$spiroH$_4$ and −1.80(1) for [{Co^{III}(tpa)}$_2$Br$_4$spiro](PF$_6$)$_2$.[24] The MOS of −1.69 to −1.76 across the temperature range indicate majority cat^{2-}, but the reduced MOS suggests some possible SQ$^{\bullet-}$ as a result of partial HS-Fe(II)-SQ character, which has been observed in the literature for mononuclear analgoues.[39,41] Upon

decreasing the temperature from 350 K to 30 K, the MOS did not approach a value closer to –2 (from −1.75 at 350 K to −1.70 at 30 K), ruling out a transition from Fe(II)-SQ at high temperature to Fe(III)-cat at low temperature (Figure S6). It is important to note that MOS is considered less reliable for electron-poor dioxolenes.[53] Overall, compound **2**·*i*Pr$_2$O·*x*H$_2$O at 350 K was found crystallographically to be in the [HS-HS] state with Br$_4$spiro^{4-} in the cat^{2-}-cat^{2-} oxidation state, with cooling to 30 K resulting in a partial SCO transition estimated to afford 25-30% of the Fe(III) sites as LS.

As mentioned, it was not possible to grow single crystals of **1**. For compound **3**, despite numerous efforts to collect higher quality data for the poorly diffracting large crystals, including multiple solvent combinations, use of synchrotron radiation,[55,56] and various collection temperatures, the data are still poor. This is most likely due to the large void space and the resultant disordered solvent and anions. At 100 K, compound **3**·Et$_2$O crystallizes in the monoclinic *I2/a* space group, with two dinuclear complexes in the asymmetric unit (four iron sites). The unit cell parameters for the collected structure are a = 43.388(6), b = 12.631(3), c = 43.784(6) Å and α = 90°, β = 90.56(3)°, γ = 90° and V = 23994(7) Å^3 (Table S2). A solvent mask regime was used to model the disordered solvent and PF_6^- anions, and based on residual volume and electron count was assigned as two PF_6^- anions and one Et$_2$O molecule per formula unit, consistent with [{Fe(tpa)}$_2$thea](PF$_6$)$_2$·Et$_2$O.

As for **2**, each Fe(III) center in **3** is coordinated by a tpa ligand and the two Fe(III) centers are bridged by a thea^{4-} ligand (Figure 1), although for **3** the two Fe(III) sites in each of the two independent dinuclear complexes are crystallographically inequivalent (Table S3, Figure S7). Caution has been taken to avoid overanalyzing the structural data due to its relatively poor quality, however the errors in the Fe−N and Fe−O distances are small enough to warrant their

consideration. Analysis of the average Fe−N and Fe−O distances reveal that each independent molecule has one Fe site with smaller and one with longer average bonds, with very similar bond lengths the two molecules (Table S3, Figure S7). The sites with longer bonds have average Fe−N/O distances of 2.071(7)-2.106(7)/1.909(7)-1.927(9) Å versus the shorter average Fe−N/O distances of 1.997(7)-2.006(7)/1.896(7)-1.897(8) Å. The Fe(III) sites with the longer bonds also display increased octahedral distortion (*SHAPE*: 1.26, 1.50) compared to the other Fe(III) sites (*SHAPE*: 0.65, 0.62). Thus the individual bond lengths within each $[\{Fe(tpa)\}_2thea]^{2+}$ molecule are consistent with one HS-Fe(III) and one LS-Fe(III) site suggesting a mixed spin [LS-HS] state for both dinuclear complexes in the structure.[34,37,41,50] The average Fe−N and Fe−O bond length difference between the two Fe(III) sites within each molecules of 0.087(7) and 0.022(8) Å, respectively, are consistent with the average difference between LS-Fe(III) and HS-Fe(III) distances in mononuclear Fe(III)-cat complexes (Fe−N: 0.06-0.14 Å; Fe−O: 0.03 Å).[34,37,41,50] Therefore, the structural parameters observed for **3**·Et_2O at 100 K are consistent with the two $[\{Fe(tpa)\}_2thea]^{2+}$ complexes in the asymmetric unit exhibiting the mixed [LS-HS] state, rather than the compound being comprised of an equal mixture of [LS-LS] and [HS-HS] states.

Infrared Spectroscopy

Infrared (IR) absorption spectra of **1**·$2H_2O$·0.5*i*Pr_2O, **2**·$1.3H_2O$, and **3**·$2H_2O$·0.5*i*Pr_2O were acquired in the solid state (ATR; 4000 – 400 cm^{-1}; Figure S8, S9), with tabulated data and assignments in Table S4. Previous DFT and transient IR studies have established the characteristic bands associated with catecholate and semiquinonate oxidation states.[57,58] The relatively intense peaks at 1280, 1253, 1284 cm^{-1} for **1**·$2H_2O$·0.5*i*Pr_2O, **2**·$1.3H_2O$, and **3**·$2H_2O$·0.5*i*Pr_2O respectively are assigned as characteristic catecholate skeletal stretches, and indicate a cat^{2-}-cat^{2-} oxidation state in the solid-state at room temperature.[44] There are no characteristic semiquinonate stretches.

For **2**·1.3H_2O, although the crystal structure suggests a MOS of –1.75 at room temperature, partial SQ character is not evident in the IRspectra, possibly due to an averaging effect. The reduced energy of the catecholate stretch for complex **2** compared to **1** and **3** arises from a weakening of the bonds induced by the inductive effect of the ligand bromo substituents. This reduced electron density on the catecholate units in **2** compared to **1** has possibilities in either reducing the σ-donating and/or π-donating capacities, affecting the ligand field strength and therefore the SCO properties. Overall, IR confirms a cat^{2-}-cat^{2-} oxidation state for the bis(dioxolene) linker in **1**·2H_2O·0.5*i*Pr_2O, **2**·1.3H_2O, and **3**·2H_2O·0.5*i*Pr_2O and the weakening of the catecholate bonds in Br_4spiro^{4-} caused by the Br groups.

Solid State Magnetic Measurements

Variable temperature magnetic susceptibility measurements were collected for solid samples of **1**·2H_2O·0.5*i*Pr_2O, **2**·1.3H_2O, and **3**·2H_2O·0.5*i*Pr_2O with an applied field of 1000 Oe. Data were collected by cooling from 300 K to 1.8 K, and then heating from 1.8 K back to 300 K. The data obtained upon first cooling and heating overlay within margin of error for all samples (Figure S10).

Compound **1**·2H_2O·0.5*i*Pr_2O exhibits a $\chi_M T$ value of 8.7 cm^3 mol^{-1} K at 300 K (Figures 3, Figure S11), consistent with two non-interacting HS-Fe(III) ($2 \times S = 5/2$, theoretical $\chi_M T = 8.75$ cm^3 mol^{-1} K), and diamagnetic ligands, decreasing very gradually to 8.1 cm^3 mol^{-1} K at 15 K, before more rapidly decreasing to 5.3 cm^3 mol^{-1} K at 1.8 K. This relatively consistent $\chi_M T$ between 15 and 300 K suggests that **1**·2H_2O·0.5*i*Pr_2O remains in the [HS-HS] state across the full measured temperature range. The very small decrease upon cooling could be due to either a small fraction of molecules undergoing SCO or to weak antiferromagnetic intramolecular coupling between the HS-Fe(III) centers. The absence of a peak in the plot of χ_M versus T tends to discount coupling as

the origin of this feature, although efforts to fit the data in the range 15-300 K to an isotropic Heisenberg exchange Hamiltonian $\hat{H}_{ex} = -2J(S_1 \cdot S_2)$ using the program PHI)[59] (Figure S11) afford best fit parameters of $g = 1.99$ and $J = -0.18$ cm^{-1}. This g-value is as expected for HS-Fe(III). The spiro^{4-} ligand is quite extended and would not be expected to afford a strong superexchange interaction, consistent with this very small coupling constant. Although there is no crystal structure of **1**, the structure of Br_4spiro^{4-} analogue **2**, indicates an intramolecular Fe···Fe separation of around 10.4 Å, so dipolar coupling would be negligible. Thus, although these data can be fit with a very small antiferromagnetic coupling constant, it is not possible to distinguish between the effects of coupling or the presence of a small amount of SCO. The rapid decrease $\chi_M T$ at low temperatures (below 15 K) has been observed previously for HS-Fe(III)-cat systems and can be ascribed to very weak intermolecular interactions and/or zero-field splitting (ZFS) effects, the latter of which potentially arises from a small fraction of HS-Fe(II)-SQ.[35,39,43] The low temperature magnetization data measured at 1.8 K do not saturate with a field up to 7 T (Figure S12) reaching a maximum value of around 8.0, which is consistent with a predominant [HS-HS] ground state with some SCO and/or ZFS .

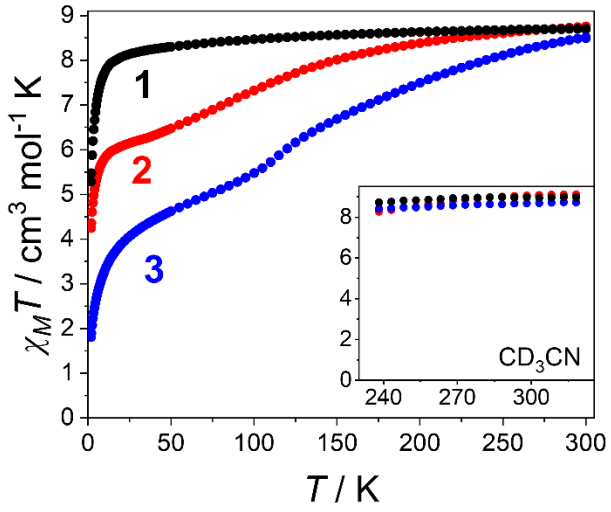

Figure 3. Plots of $\chi_M T$ vs T for **1**·2H$_2$O·0.5*i*Pr$_2$O (black), **2**·1.3H$_2$O (red), and **3**·2H$_2$O·0.5*i*Pr$_2$O (blue). Inset: Plots of $\chi_M T$ vs T for solution state magnetic data for **1** (black), **2** (red), and **3** (blue) in d$_3$-MeCN

Compounds **2**·1.3H$_2$O and **3**·2H$_2$O·0.5*i*Pr$_2$O exhibit 300 K $\chi_M T$ values of 8.7 and 8.5 cm^3 mol^{-1} K, respectively (Figure 3), again consistent with two non-interacting HS-Fe(III). Upon cooling **2**·1.3H$_2$O, there is a steady decrease to 6.1 cm^3 mol^{-1} K at 25 K, with the first derivative plot suggesting an inflection point around 85 K (Figure S13). Upon cooling **3**·2H$_2$O·0.5*i*Pr$_2$O, there is a more rapid decrease to 6.2 cm^3 mol^{-1} K centered at 115 K (Figure S13), before an abrupt decrease to reach 5.3 cm^3 mol^{-1} K at 90 K. This is followed by a continual gradual decrease to reach 4.1 cm^3 mol^{-1} K at 25 K. These observed decreases in $\chi_M T$ are consistent with incomplete SCO interconversions for both compounds. Below 25 K, the $\chi_M T$ for **2**·1.3H$_2$O and **3**·2H$_2$O·0.5*i*Pr$_2$O rapidly decreases to 4.3 and 1.8 cm^3 mol^{-1} K at 1.8 K, respectively, in a similar fashion to **1**·2H$_2$O·0.5*i*Pr$_2$O.

It is important to consider the possibility of exchange coupling of the Fe(III) centers in the dinuclear complexes, but it is challenging to do this quantitatively in the presence of SCO. The theoretical $\chi_M T$ values for the [HS-HS], [LS-HS] and [LS-LS] states with no magnetic coupling (ie Curie behavior) are 8.8, 4.8 and 0.75 $cm^3\ mol^{-1}\ K$, respectively. If magnetic exchange is occurring between the Fe(III) centers, deviation from the theoretical $\chi_M T$ values will be observed. Considering that for the [HS-HS] state for **1**, the experimentally determined J value is very small, and similarly weak exchange was calculated for the [HS-HS] states of **1**, **2** and **3** ($J = -1, -2, -6$ cm^{-1}, respectively, see DFT section later), the [HS-HS] state will display a $\chi_M T$ value close to 8.8 $cm^3\ mol^{-1}\ K$ for all complexes. Regarding the [LS-HS] state, we were unable to determine the J values experimentally, however the calculated J values for the LS-HS state are −2, 0 and −55 (see DFT section) for **1**, **2** and **3**, respectively. Thus, the theoretical $\chi_M T$ for this state would be close to 4.8 $cm^3\ mol^{-1}\ K$ for **1** and **2,** with deviations for **3** at lower temperature. Regarding [LS-LS], calculated larger J values of −12, −11 and −281 cm^{-1} (see DFT section) for **1**, **2** and **3**, respectively, would result in $\chi_M T$ approaching 0 $cm^3\ mol^{-1}\ K$ at low temperatures.

The $\chi_M T$ value reached by **2**·1.3H_2O of 6.2 $cm^3\ mol^{-1}\ K$ at 30 K lies between the theoretical values of [HS-HS] and [LS-HS] assuming no exchange. For **3**·2H_2O·0.5*i*Pr_2O, the $\chi_M T$ of 4.3 $cm^3\ mol^{-1}\ K$ at 30 K is consistent with the theoretical value for [LS-HS] with no exchange. Neither **2**·1.3H_2O nor **3**·2H_2O·0.5*i*Pr_2O reach a $\chi_M T$ value consistent with [LS-LS] without exchange (0.75 $cm^3\ mol^{-1}\ K$), or with strong antiferromagnetic (0 $cm^3\ mol^{-1}\ K$) or ferromagnetic (1.0 $cm^3\ mol^{-1}\ K$) exchange. Therefore, assuming no or very small magnetic coupling, the extent of SCO conversion observed for **2**·1.3H_2O and **3**·2H_2O·0.5*i*Pr_2O can be approximated to 33% and 50% conversion, respectively, from the room temperature [HS-HS] state. For a dinuclear complex, the plateau in a two-step profile can arise from [LS-HS] or an equal mixture of [HS-HS] and [LS-LS].

Examples of both situations have been reported in the literature,[26,60] and deducing the exact nature of the transition is non-trivial. The structural analysis of **3**·Et_2O at 100 K suggests a [LS-HS] state and, given the clear plateau at low temperatures at essentially the theoretical $\chi_M T$ value for [LS-HS] for **3**·2H_2O·0.5*i*Pr_2O, a [HS-HS] ⇌ [LS-HS] SCO transition is probable. For **2**·1.3H_2O, the low temperature plateau could therefore arise from a mixture of [LS-HS] and [HS-HS] states. The SCO transition for **2**·1.3H_2O is consistent with the variable temperature crystallographic data for **2**·*i*Pr_2O·*x*H_2O from 350 to 30 K (Figure S14). It is possible that the localization of the PF_6^- anion observed crystallographically from 150 to 100 K is correlated with the SCO transition which begins to accelerate below 150 K. However, the localization at 100 K might be due to reduced PF_6^- rotation at low temperature. Finally, the low temperature magnetization data measured at 1.8 K do not saturate with a field up to 7 T for any of the three complexes (Figure S12). The maximum magnetization values of 8.0, 6.4 and 3.8 for **1**·2H_2O·0.5*i*Pr_2O, **2**·1.3H_2O and **3**·2H_2O·0.5*i*Pr_2O, respectively, are consistent with predominant [HS-HS] and [LS-HS] ground states for **1** and **3** with **2** comprised of a mixture of these two states.

Overall, in the solid-state, all structural and magnetic data are consistent with **1**·2H_2O·0.5*i*Pr_2O remaining [HS-HS], **2**·1.3H_2O undergoing a SCO to yield a mixture of [HS-HS] and [LS-HS], and **3**·2H_2O·0.5*i*Pr_2O undergoing near complete SCO conversion to mixed [LS-HS] state. The nature of the bis(catecholate) bridging ligand significantly affects the observed SCO behavior in the solid state.

Electronic Spectroscopy

Compounds **1**, **2** and **3** are unstable to air in solution. Thus, all solution magnetic, spectroscopic and electrochemical measurements on **1**, **2** and **3** were performed on samples prepared under a N_2

atmosphere (glovebox) using degassed and dry solvent and carried out in appropriate anerobic cells or tubes. Ultraviolet-visible-near-infrared (UV-Vis-NIR) absorption spectra were recorded for compounds **1**, **2** and **3** at room temperature in MeCN, butyronitrile (BuCN), and dichloroethane (DCE) (Figure 4, Figure S15, Table 2). In solution, the spectra remained unchanged over several hours (when prepared under inert conditions), consistent with solution stability. In MeCN, the visible region of the spectra of **1**, **2** and **3** is dominated by broad bands centered at ~860-1020 and ~520-600 nm (Figure 4, Table 2) that arise from a $cat^{2-} \rightarrow$ LS-Fe(III) ligand-to-metal charge transfer (LMCT).[34,39,40] These LMCT bands are influenced slightly by solvent choice, shifting to lower energies for all three complexes following MeCN > BuCN > DCE. Previous red shifting of similar Fe(III)-catecholate LMCT bands in chlorinated solvents has been observed previously.[35,61] The lowering of energy of this LMCT follows the trend of decreasing dielectric constant of the solvent (MeCN = 37.5, BuCN = 10.7, DCE = 10.3), and likely arises from the increased stabilization of the Fe(II)-SQ state which has a smaller dipole compared to Fe(III)-cat.[61,62] Across MeCN, BuCN and DCE, the dominant LMCT band shifts to lower energy following **2** > **1** > **3**. The increased energy of the LMCT in **2** results from the electron-withdrawing Br groups on the Br_4spiro^{4-} bridging ligand. This mirrors **2** displaying the lowest energy catecholate stretch in the IR spectra. No major peaks in the NIR region are observed that would originate from mixed-valency in the bridging bis(dioxolene) ligand in all complexes, confirming a cat^{2-}-cat^{2-} state in solution at room temperature. Small shoulders at ~1100-1200 nm for **1**, **2** and **3** in all solvents are observed, and arises from a LMCT from cat^{2-} to LS-Fe(III),[39,41,63] suggesting all compounds include a minor LS containing state in solution at room temperature.

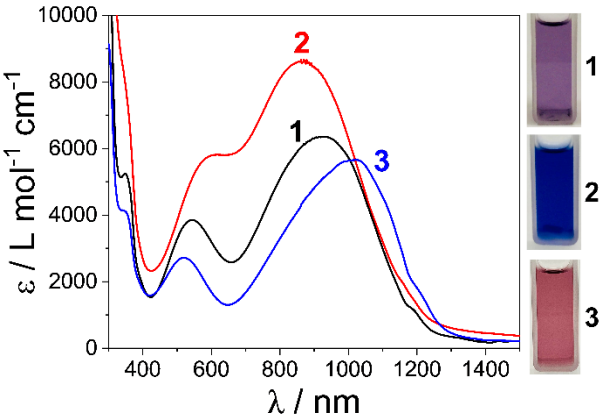

Figure 4. UV-Vis-NIR absorption spectra and photographs of acetonitrile solutions of **1**, **2** and **3** at 298 K.

Table 2. Wavelength (nm) of dominant LMCT band in **1**, **2** and **3** in MeCN, BuCN and DCE.

	1	**2**	**3**
MeCN	916	868	1020
BuCN	956	890	1042
DCE	979	910	1054
Solid state	947	852	971

In the solid-state diffuse reflectance spectra, the LMCT bands also dominate the spectra for **1**·2H_2O·0.5*i*Pr_2O, **2**·1.3H_2O and **3**·2H_2O·0.5*i*Pr_2O (Figure S16), with the same energy trend as observed in solution. At room temperature, the electronic state adopted by all three compounds is the same in solution as in the solid state; i.e [HS-HS] and the bis(dioxolene) in the cat^{2-}-cat^{2-} oxidation state.

Variable Temperature Solution Measurements

In the solid state, the SCO properties of a compound can be affected by crystal packing, solvation, and intermolecular interactions. In solution, these complications are removed, allowing for a direct analysis of the effect the ligands have on the SCO properties. Solution magnetic susceptibility measurements of **1**, **2** and **3** were conducted using the Evans NMR method with d_3-acetonitrile solutions between 238 and 318 K, as limited by the freezing and boiling temperatures (Figure 3).[64] At 318 K, complexes **1**, **2** and **3** displayed $\chi_M T$ values of 9.0, 9.1 and 8.7 $cm^3\ mol^{-1}\ K$, respectively, indicative of a [HS-HS] state. Upon cooling, all three complexes display a gradual decrease in $\chi_M T$ to 8.7, 8.3 and 8.4 $cm^3\ mol^{-1}\ K$ at 238 K for **1**, **2** and **3** respectively. This represents only the very onset of SCO in MeCN for all complexes. With the current presented data, we are unable to determine the nature of the SCO for each individual complex in solution. We attempted solution SQUID measurements; unfortunately, the low solubility of **1**, **2** and **3** limited the concentration of the measured solutions resulting in poor data. It is clear that, at room temperature, all three complexes are in the [HS-HS] state in MeCN, as suggested by UV-Vis-NIR, and upon cooling the beginning of SCO is observed.

Variable-temperature UV-Vis spectra were recorded for **1**, **2** and **3** to study the spectral changes upon SCO interconversion in solution. Spectra was recorded in MeCN (273 – 338 K), BuCN (273 – 358 K) and DCE (273 – 328 K) (Figure 5, Figure S17) to study the solvent effect. The 298 K spectra was recovered for each complex in each solvent after the full temperature measurement (Figure S18 – S20), indicating reversible interconversions and thermal stability of the complexes. Distinct and reversible spectral changes are evident for **1**, **2** and **3** in all three solvents as expected for a SCO transition. In MeCN, an isosbestic point at 1000, 975, and 1040 nm for **1**, **2** and **3** respectively are observed, indicating multiple absorbing species. Compounds **1** and **3** also have additional isosbestic points at 595 and 640 nm, and 555 and 660 nm respectively.

The number and general energy of these isosbestic points for **1** and **3** are conserved in BuCN and DCE. Upon increasing temperature from 273 K **1**, **2** and **3** in MeCN, BuCN and DCE, the LMCT bands decrease in intensity and red shift. The observed changes to the LMCT differ from analogous mononuclear complexes (that incorporate 4-chlorocatechol and different substituted tpa ligands), which saw a decrease and increase in intensity of the high energy LMCT and low energy LMCT upon increasing temperature, as well as a blue shift.[39] The spectral changes observed are small for all complexes, but reproducible and consistent with each other. This agrees with the solution magnetic data, which showed that all three complexes remain predominantly in the [HS-HS] state between 273 and 320 K and only the onset of SCO occurs upon cooling. Between solvents, no discernable difference is observed, indicating that SCO for **1**, **2** and **3** in solution is only marginally affected by solvent choice.

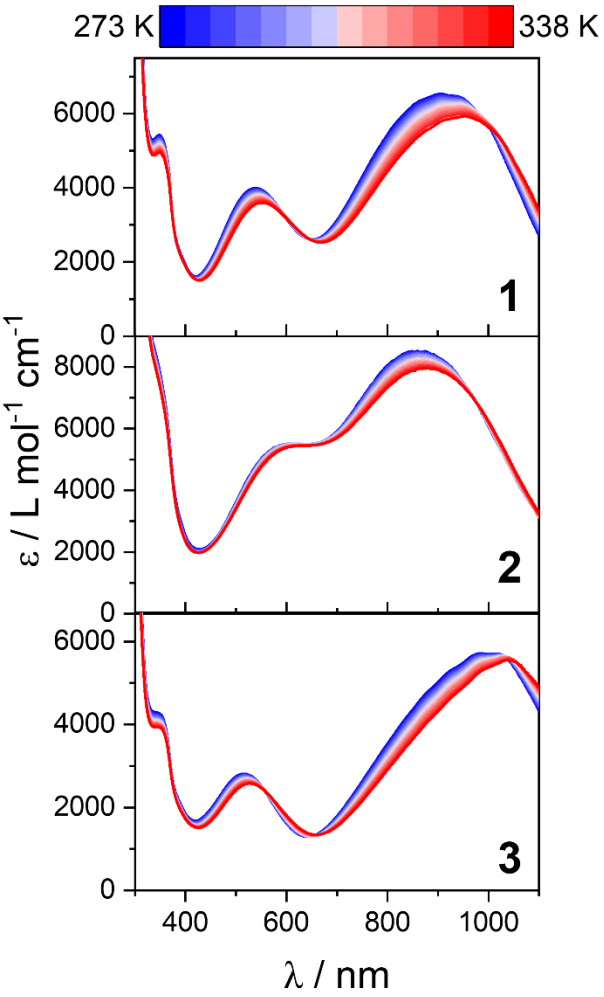

Figure 5. Variable temperature absorption spectra of **1**, **2** and **3** in MeCN between 273 (blue) and 338 K (red) in 5 K increments.

To aid in the determination of the ground state of **1**, **2** and **3** in solution, we performed CW X-band EPR measurements of the three compounds in a 40:60 MeCN:toluene solution at room temperature and 77 K. For literature mononuclear analogues, the LS-Fe(III) (S = 1/2) species is characterized by a pseudo-axial spectrum with reported g values of $g_{\perp}$ = 2.12–2.35 and $g_{\parallel}$ = 1.83–1.98,[20,38,39,43] with the difference between $g_{\perp}$ and $g_{\parallel}$ indicating the degree of anisotropy that arises from mixing of Fe(III)-cat and Fe(II)-SQ.[38] For the HS-Fe(III) (S = 5/2) state in the mononuclear

analogues, a signal is observed at low fields (~150 mT), broadened by spin-spin interactions.[20,39] At room temperature, **1**, **2** and **3** exhibit no EPR signals, presumably due to fast relaxation. Upon cooling to 77 K, the spectra for **1**, **2** and **3** show HS signals at around $g \sim 4.3$ and LS signals at around $g \sim 2$ (Figure S21). These signals are broad, likely in part due to the MeCN/toluene mixture crystallizing upon freezing and/or exchange interactions or strains from variations in molecular geometries. The spectra for **1** and **2** contain similar features. The LS signal appears to have contributions from at least two species, giving rise to a sharper rhombic and broader isotropic signal, possibly due to combination of [LS-HS] and [LS-LS] species or a [LS-HS] state complicated by freezing. The broad HS signal also appears to have contributions from two species, possibly [HS-HS] and [LS-HS]. For **3**, a large sharp LS signal, most likely arising from a mixture of LS-LS and LS-HS, is observed along with a very weak HS signal. The LS signal appears consistent with the LS state in mononuclear analogues.[20,38,39,43] Therefore, in solution at 77 K, the EPR spectra suggest that **1**, **2** and **3** are undergoing SCO, with complexes **1** and **2** appearing to contain a mixture of [LS-LS], [LS-HS] and [HS-HS], and complex **3** containing [LS-LS] and [LS-HS].

We have attempted to fit the spectra for **1**, **2** and **3**, however no satisfactory fit was obtained. Therefore, the reported *g* values are estimates. It is not possible with the current data to quantitatively compare the amount of HS and LS for the three complexes. However, some trends are apparent regarding the extent of SCO transition. At 77 K, **1**, **2** and **3** display signals that can be attributed to [LS-LS], suggesting that in solution the ground state for all three complexes is [LS-LS]. It is also possible that signals arising for a [LS-HS] state are also observed. Comparing the untransformed signal integrals for **1**, **2** and **3** (Figure S21), the relative amount of LS vs HS increases in the order **1** < **2** < **3**, indicating that ligand field strength increases in the order spiro^{4-}

< Br_4spiro^{4-} < thea^{4-}. For **3**, the $g_\perp - g_\parallel$ of ~0.22 is comparable to [Fe^{III}(tpa)(3,5-dbcat)]$^+$ (3,5-dbcat^{2-} = 3,5-di-*t*Bu-catechol) ($g_\perp - g_\parallel$ = 0.223) but larger than for [Fe^{III}(tpa)(3,6-dbcat)]$^+$ (3,6-dbcat^{2-} = 3,6-di-*t*Bu-catechol) ($g_\perp - g_\parallel$ = 0.136), indicating similar amounts of Fe(II)-SQ contribution for **3** that is evident for [Fe^{III}(tpa)(3,5-dbcat)]$^+$.[38,43] In summary, the EPR spectra are consistent with **1**, **2** and **3** adopting a [HS-HS] state at room temperature, with a [LS-LS] state apparent upon cooling. The proportion of [LS-LS] at 77 K increases in the order **1** < **2** < **3**, correlating with the increasing ligand field strength of the bis(catcholate).

Electrochemistry

The redox properties of complexes **1**, **2** and **3** were investigated by cyclic voltammetry (CV) and rotating disk electrode (RDE) voltammetry in MeCN solutions (Figure 6, Table 3) under N_2. Before electrochemical studies, the compounds stability in solution under N_2 was confirmed via electronic absorption spectroscopy over time. The mid-point potentials (E_m) were determined by taking the average of the peak anodic potential (E_{pa}) and peak cathodic potential (E_{pc}) from the CV (Table 3). The peak potential (E_p) is reported in the case of irreversible processes. Where possible, the peak separation (ΔE_p), between the E_{pa} and E_{pc} is given. From RDE, the half-wave potentials ($E_{1/2}$) and limiting curents (i_L) are reported.

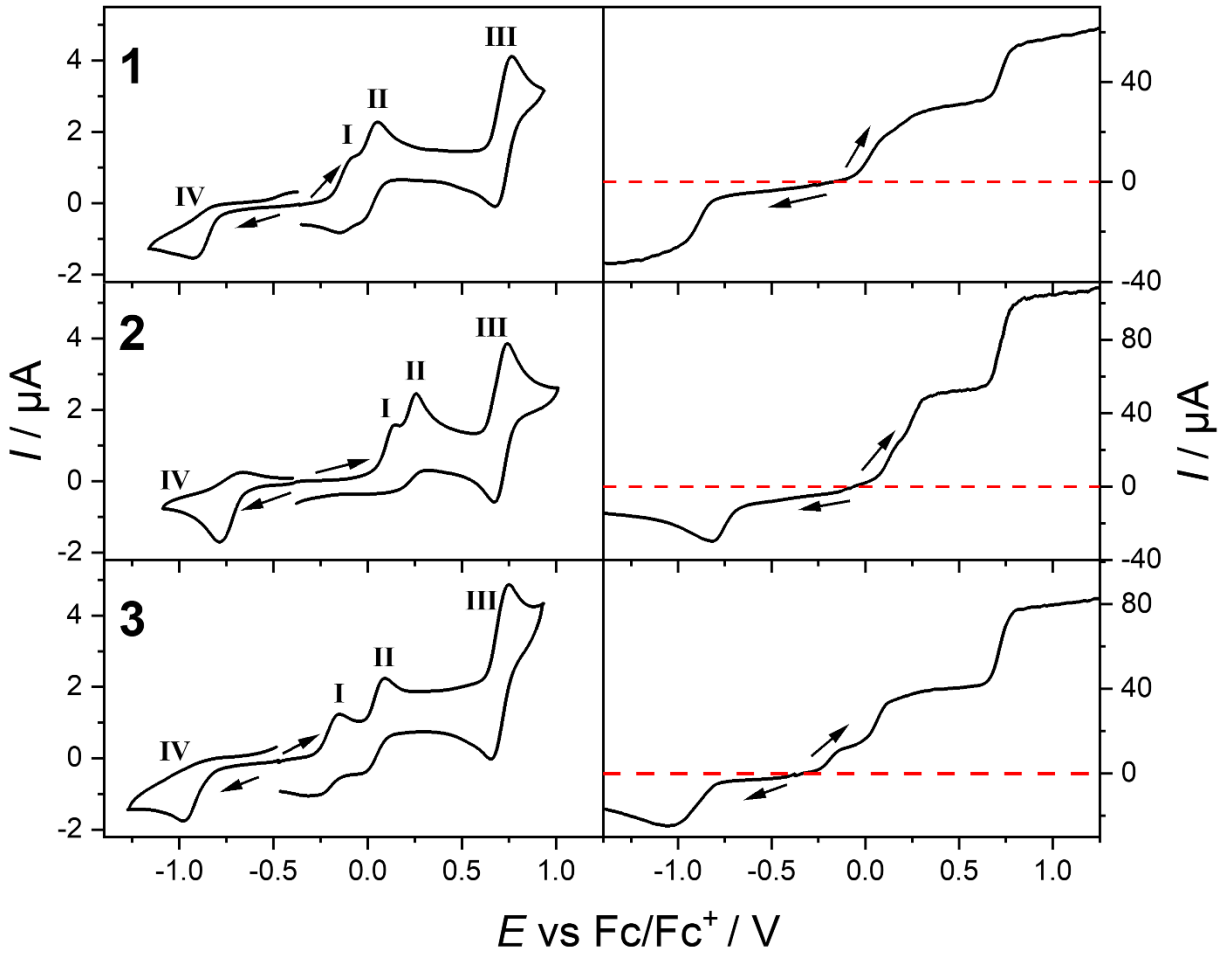

Figure 6. (Left) Cyclic voltammograms of MeCN solutions of compounds **1**, **2** and **3** (1.0 mM with 0.25 M Bu_4NPF_6) obtained with a scan rate of 100 mV s^{-1}. (Right) Corresponding RDE voltammograms at a scan rate of 50 mV s^{-1} and a rotation rate of 500 rotations min^{-1}. Arrows indicate the starting point and direction of the scan.

Table 3. Cyclic Voltammetry and Rotating Disk Electrode Voltammetry Data for Compounds **1**, **2**, **3** in MeCN[a]

	Cyclic Voltammetry E_m or E_{pa} / V (ΔE_p / mV)[b]				**Rotating Disk Electrode Voltammetry $E_{1/2}$ / V (i_L / μA)[c]**		
	I	II	III	IV	I	II	III
1	−0.125 (55)	0.023 (60)	0.720 (85)	−0.930[d]	0.054 (27)[e]		0.725 (21)
2	0.146[d]	0.256[d]	0.706 (70)	−0.784[d]	0.180 (49)[e]		0.721 (48)
3	−0.231 (168)	0.041 (103)	0.703 (95)	−0.980[d]	−0.195 (10)	0.057 (18)	0.718 (35)

[a] Potentials reported vs Ferrocene/Ferrocenium couple. Error in potentials is ±5 mV. [b] 1.0 mM in MeCN with 0.25 M Bu_4NPF_6, scan rate 100 mV s^{-1}. [c] 1.0 mM in MeCN with 0.25 M Bu_4NPF_6, scan rate 50 mV s^{-1} and 500 rotations min^{-1}. Process IV not included due to inversible nature precluding fit. [d] E_p rather than E_m. [e] Processes combined due to close spacing.

The voltammograms of **1**, **2** and **3** all display four redox events: two closely spaced one electron oxidations processes (I and II), a two-electron oxidation process (III) and a single reduction (IV) (Figure 6, Table 3). The RDE position of zero current confirms I, II and III as oxidation processes, and IV as a reduction. Process I and II are irreversible for **2** and quasi-reversible for **1** and **3**, process III is reversible in all three compounds (same ΔE_p as ferrocene under the same conditions), and process IV is irreversible for all three compounds. Processes I and II are assigned as sequential one electron oxidations of the bis(dioxolene) bridging ligand from cat^{2-}-cat^{2-} to SQ-cat to $SQ^{\bullet-}$-$SQ^{\bullet-}$ (Scheme 2). Process III is assigned as a two-electron oxidation of the bis(dioxolene) from $SQ^{\bullet-}$-$SQ^{\bullet-}$ to Q-Q (Q = quinonate). Process IV is assigned as a two-electron reduction of both Fe(III) centers to Fe(II).

Scheme 2. Assigned redox processes for compounds **1**, **2** and **3**.

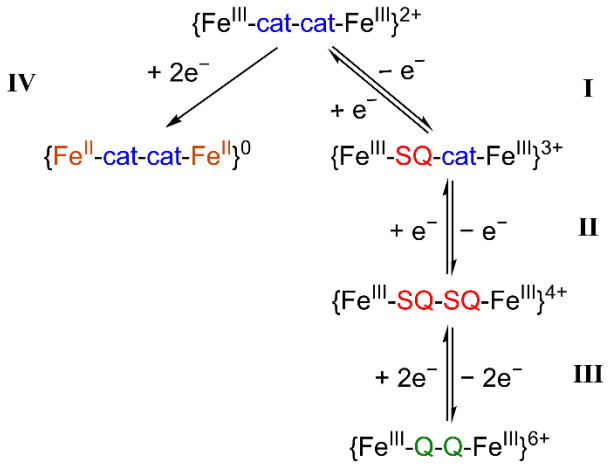

Comparing the voltammograms of **1** and **2,** the redox potential for processes I and II are shifted approximately +250 mV as electron-withdrawing bromo groups are introduced in **2**, indicative of a higher energy highest occupied molecular orbital (HOMO) in **2** compared to **1**. As process I and II are irreversible in **2**, the RDE voltammetry data was also used to compare the average potential difference, giving a value of +230 mV. For compound **3**, the CV process I is shifted approximately −100 mV compared to **1**, whilst process II in **3** is relatively similar that of **1**, with the average of process I and II for **1** and **3** of −0.05 and −0.1 V, respectively, being similar within error. In the RDE, the average potential of I and II for **1** and **3** of 0.05 and 0.07 V confirms this similarity. The lower redox potential of process I, and thus easier oxidation, of the bis(catecholate) following **3** < **1** < **2** is manifested in their visual solution air-sensitivity; **2** is stable for an hour, **1** for a few minutes and **3** for a few seconds. The potential for process IV for **1**, **2** and **3** of −0.9, −0.8 and −1.0 V, respectively, indicates that Br_4spiro^{4-} stabilizes the Fe(II) state to the greatest extent, presumably due to the inductive nature of the bromo substituents. The separation

between the first bis(dioxolene) oxidation and Fe(III) reduction of ~800, 930 and 750 mV for **1**, **2** and **3**, respectively, indicates the closest metal-ligand orbital energy match for **3**, and mirrors the observed decrease of the LMCT observed in the UV-Vis-NIR following **2** > **1** > **3**.

The electronic communication between the dioxolene moieties in bis(dioxolene) ligands can be correlated with the separation between the two sequential 1e-oxidation of the bis(dioxolene) ligands (processes I and II) with the relevant parameter defined as Δ*diox*.[24] The larger the Δ*diox*, the stronger the communication between the metal centers mediated via the bridging ligand. The Δ*diox* values for **1**, **2** and **3** are ~150, 110 and 270 mV, respectively. The Δ*diox* values for **1** and **2** are comparable within error and are similar to the values of 160 and 135 mV reported for the cobalt analogues of **1** and **2**, respectively. The Δ*diox* value of 270 mV for **3** indicates that the thea^{4-} ligand affords increased communication compared to spiro^{4-} and Br$_4$spiro^{4-}, consistent with previous literature observations.[24,65] Calculations of the relevant comproportionation constants (K_{comp}) using Δ*diox* and $\log_{10}(K_{comp}) = 17.2 \times \Delta diox$ (Δ*diox* in V) yielded values of 35, 80, and 47,700 for **1**, **2** and **3** respectively.[44,66] A through-space origin for the stronger communication in thea^{4-} compared to spiro^{4-} and Br$_4$spiro^{4-} can be discounted as the average intramolecular Fe-Fe distance in **2** and **3** are 10.4 and 11.6 Å, respectively. Instead, the dimethyl-bicyclo[2.2.2]octyl spacer in thea^{4-} must mediate better orbital overlap between the two dioxolene units compared to the spirocyclic carbon bridge in spiro^{4-} and Br$_4$spiro^{4-}.

Overall, **1**, **2** and **3** display sequential bis(dioxolene) cat^{2-}-cat^{2-} ⇌ SQ$^{\bullet-}$-cat^{2-} ⇌ SQ$^{\bullet-}$-SQ$^{\bullet-}$ oxidations, a SQ$^{\bullet-}$-SQ$^{\bullet-}$/Q-Q oxidation, and an Fe(III)/Fe(II) reduction. The sequential bis(dioxolene) oxidations are shifted to higher potential for **2** compared to the relatively similar **1** and **3**, a result from the bromo substituents. The separation of the bis(dioxolene) processes is small

for **1** and **2**, but relatively larger for **3**, indicating a larger orbital overlap between the two dioxolene units and therefore stronger communication within thea^{4-} for complex **3**.

Density Functional Theory Calculations

Density functional theory (DFT) calculations were performed for compounds **1**, **2** and **3** in the gas phase, and taking into account nonspecific solvation (SMD) (solvent – acetonitrile),[67] to examine the relative energies of the [HS-HS], [LS-HS], and [LS-LS] spin states. The DFT calculations were performed using the Gaussian 16 program package[68] with the UOPBE[69,70] functional and the standard 6-311++G(d,p) basis set including diffuse and polarization functions at all atoms. Mononuclear Fe(III)-cat systems have been investigated with DFT,[35,41,43] but to date, DFT calculations on dinuclear Fe(III)-catecholate compounds have been applied only to hypothetical complexes.[71,72]

Previous work on mononuclear Fe(III)-cat systems utilized the UTPSSh functional, which has performed well in VT and SCO complexes.[24,35,73,74] However, for Fe(III)-cat complexes, UTPSSh/6- 311++G(d,p) calculations have overstabilized the LS-Fe(III) state energy, inconsistent with experimental evidence.[35,41] Instead, the cost-effective OPBE functional has recently been successful in accurately capturing the energetics of the spin states in Fe(II) and Fe(III) SCO complexes,[75–77] and UOPBE/6-311++G(d,p) has correctly calculated the energies of the spin states in Fe(III)-cat systems for which UTPSSh was unsuccessful.[71] In this work, calculations were performed with UOPBE/6-311++G(d,p). The stationary points on the potential energy surfaces (PES) were localized by a full geometry optimization (Figure S22 – S24), with subsequent confirmation of the stabilities of the DFT wave function and calculation of the force constant matrices. For compounds **2** and **3**, crystallographic data were used for the geometry optimization,

while the geometry of compound **1** was derived from that of **2**. Previous studies with related dinuclear cobalt complexes have shown similar molecular structures for complexes with spiro^{4-} and Br$_4$spiro^{4-}.[24] All calculations included the PF_6^- anions, which has been shown previously to aid in the correct calculation of the spin state energetics.[78–80]

The calculated Fe−N/O bond lengths for the geometry optimized [HS-HS] state of **2** match best with the corresponding experimental high temperature bond lengths for **2**·*i*Pr$_2$O·*x*H$_2$O (Figure 7, Figure S25), with the average calculated Fe−O and Fe−N bond lengths for the geometry optimized [HS-HS] state of **2** of 1.97 and 2.21 Å, respectively, comparing very well to the 1.93 and 2.16 Å average bond lengths at 350 K. As well, the calculated average *SHAPE*, Σ and Θ values of 2.081, 105.1° and 314.1°, respectively, compare very well with the equivalent experimental values for the 350 K structure for **2**·*i*Pr$_2$O·*x*H$_2$O (1.925, 102.9°, 298.6°, Table 1). The average calculated Fe−O and Fe−N bond lengths for the geometry optimized [LS-HS] state of **2** of 1.93 and 2.10 Å compare well to the 1.91 and 2.12 Å bond lengths of the 30 K structure of **2**·*i*Pr$_2$O·*x*H$_2$O (Figure 7, Figure S25). The average of the Fe−O and Fe−N bond lengths in the calculated [HS-HS] and [LS-LS], and [HS-HS] and [LS-HS] states also match with the 30 K structure of **2**·*i*Pr$_2$O·*x*H$_2$O (Figure S26).

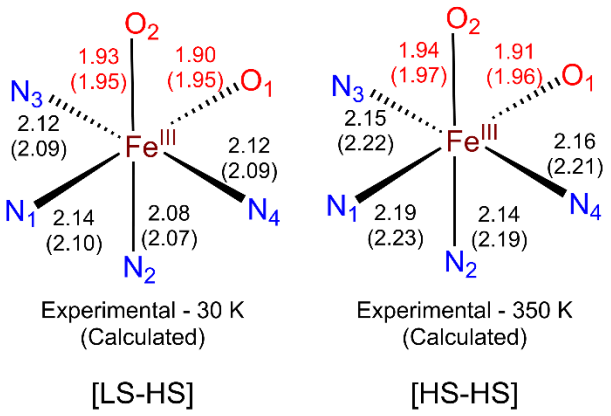

Figure 7. Comparison of the experimental bond length at 30 (left) or 350 (right) K for compound **2**·*i*Pr$_2$O·*x*H$_2$O with the gas phase calculated bond length values for [LS-HS] and [HS-HS] spin states for compound **2.** Experimental values listed above and calculated values listed below in brackets.

As expected, the calculated spin density for all three spin states for compounds reside primarily on the Fe(III) sites (Figure S27). For the [HS-HS] state, each Fe(III) center has a spin density (q_s) of 3.6, in the [LS-HS] state $q_s^{Fe1} = 0.5$ and $q_s^{Fe2} = 3.6$, and in the [LS-LS] state both sites have $q_s = 0.5$ (Table S5). The spin density for the HS-Fe(III) and LS-Fe(III) sites is lower than the expected values of 5 and 1, respectively. Coupled with the presence of spin density on the coordinating oxygen atoms (0.33 for HS-Fe(III), 0.27 for LS-Fe(III)), we can assign some Fe(II)-SQ character for **1**, **2** and **3** in all three states. For the mononuclear compound [Fe^{III}(tpa)(3,6-dbcat)]$^+$, the LS-Fe(III) spin densities were previously calculated as $q_s^{Fe} = 0.46$ and $q_s^{O} = 0.38$, indicating a smaller relative amount of Fe(II)-SQ in **3**.[43] This is consistent with the larger $g_\perp - g_\parallel$ value of **3** measured from EPR. Attempts to calculate the energy of isolated Fe(II)-SQ states

invariably led to the calculation of HS-Fe(III) instead; using single-determinant DFT approach cannot separate these states, and as such an averaged isomer is calculated.

The exchange coupling parameter J ($-2J\hat{S}_1 \cdot \hat{S}_2$ formalism), estimated using the broken symmetry approximation (Table S5)[81] was calculated to be antiferromagnetic for all three spin state for **1**, **2** and **3**. The larger values for **3** (−6, −55, −281 cm^{-1} for [HS-HS], [LS-HS] and [LS-LS], respectively) contrast to the more similar values for **1** (−1, −2, −12 cm^{-1} for [HS-HS], [LS-HS] and [LS-LS], respectively) and **2** (−2, 0, −11 cm^{-1} for [HS-HS], [LS-HS] and [LS-LS], respectively) and are consistent with stronger electronic communication mediated by $thea^{4-}$ compared to weaker communication for $spiro^{4-}$ and Br_4spiro^{4-}. It should be noted that while the signs and relative ordering of these calculated coupling constants are likely reliable, the accuracy of the absolute values is uncertain.[82–86]

Calculations on **1**, **2** and **3** indicate the structure on the triplet PES, corresponding to the [LS-LS] state, is the ground state in all three cases (Figure 8, Table S5, S6). The next highest energy electromer for the three compounds is the [LS-HS] state (septet PES) destabilized by 1.7, 1.9 and 2.1 kcal mol^{-1} for **1**, **2** and **3** respectively, followed by the [HS-HS] state (undecet PES) destabilized by 3.5, 4.0 and 4.7 kcal mol^{-1} respectively. A [LS-LS] ground state, with the [LS-HS] and [HS-HS] states destabilized by no more than 12 kcal mol^{-1},[24,87] suggests that thermally-induced SCO is accessible for **1**, **2** and **3**, which is consistent with the solution-state magnetic measurements, variable temperature UV-Vis-NIR and EPR studies for all three complexes, as well as the solid-state magnetic data for **2** and **3**. The DFT calculations do not reflect the ground states of **1**, **2** and **3** observed by magnetometry in the solid state. However, solid state SCO behavior is affected by intermolecular interactions and packing effects. Calculations are performed in the gas

phase and with accounting nonspecific solvation, and therefore neglect solid-state packing effects. From the solution EPR spectra at 77 K, [LS-LS] signals were present for **1**, **2** and **3**, suggesting a [LS-LS] ground state for all three complexes. As well, the experimental observation of the onset of SCO upon cooling solutions of all three compounds is not inconsistent with the calculated [LS-LS] ground states.

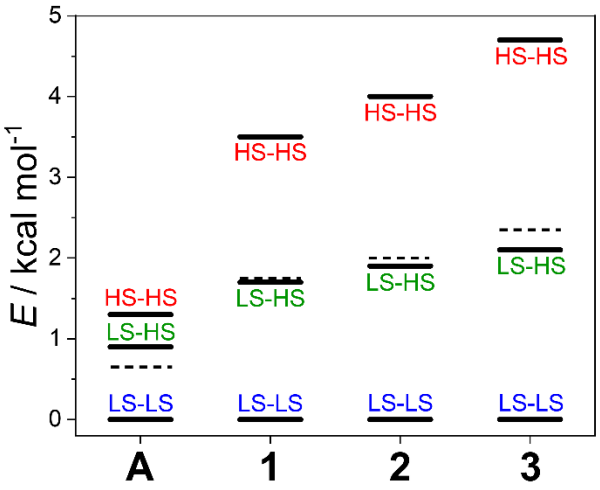

Figure 8. Plots of relative energies of different electronic states for compounds **1**, **2** and **3** studied in this work, and compound [{Fe^{III}(tpa)}$_2$6,6′-[piperazine-1,4-diyl-bis(methylene)]bis[3,5-di-tert-butyl-pyrocatechol](PF_6)$_2$ (**A**)[71] calculated by the DFT UOPBE/6-311++G(d,p) method. Dashed lines correspond to the halfway *E* between the [HS-HS] and [LS-HS] states ($\Delta H/2$).

Comparing the relative energies of the spin states for **1**, **2** and **3** provides information regarding the ligand field strength of the bis(catecholate) ligands (Figure 8, Table S5, S6). Comparing complexes **1** and **2**, the relative energies of the [HS-HS] and [LS-HS] states are higher

for **2**. The Br_4spiro^{4-} ligand must therefore provide a stronger ligand field than $spiro^{4-}$ as a result of weaker π-donation due to the inductive nature of the bromo groups. This effect is observed experimentally in the solid state: **1** remains [HS-HS] while **2** undergoes SCO. Calculations show that the [HS-HS] and [LS-HS] states are further destabilized for compound **3** compared to **2**, indicating that $thea^{4-}$ provides the strongest ligand field of the three bis(catecholate) ligands studied. The increasing ligand field in the order $spiro^{4-} < Br_4spiro^{4-} < thea^{4-}$ is consistent with the suggested ligand field trend from the solution EPR spectra at 77 K.

For dinuclear SCO complexes, the likelihood of a two-step [LS-LS] ⇌ [LS-HS] ⇌ [HS-HS] transition occurring via a mixed [LS-HS] state can be described by the thermochemical parameter ρ, calculated by $\rho = W/\Delta H$ where ΔH is the enthalpy difference between the [LS-LS] and [HS-HS] states, and W is the energetic stabilization of the [LS-HS] state relative to the average energy of the [HS-HS] and [LS-LS] states ($\Delta H/2$).[26,29,88] A negative ρ is required for a complex to display two-step SCO (i.e the [LS-HS] energy lies below the halfway energy of [LS-LS] and [HS-HS]), with a more negative ρ implying a higher chance of observing a [LS-HS] state experimentally. Compounds **1**, **2** and **3** have ρ values of −0.014, −0.025 and −0.053, respectively, which implies that all three complexes have accessible mixed [LS-HS] states, though the ρ values are comparatively small.[26,29,88] Evidence from the EPR spectra at 77 K suggests observation of [LS-HS] bands in solution for all complexes. Compound **3** has the most negative ρ value and therefore the most stabilized mixed [LS-HS] state. This is consistent with the low temperature experimental solid-state data, which indicate a [LS-HS] state for **3**, while **2** exists as a mixture of [LS-HS] and [HS-HS]. Variable temperature Mossbauer spectroscopy in an applied magnetic field would be required to confirm this.[26]

As shown by Cirera and Ruiz for dinuclear Fe(II) systems,[29] the presence or absence of a well-defined mixed-spin state intermediate species and a two-step SCO profile is dependent on the local electronic structure of the Fe(II) centers provided by the ligands. The degree of cooperativity between the Fe(II) centers plays a much smaller role than previously thought,[21,22,26,27] evidenced by the lack of change in distortion of one Fe(II) site upon SCO at the other.[29] The same observation can be made from the DFT optimized structures for **1**, **2** and **3**; when one metal undergoes SCO, the other Fe(III) site remains insensitive to that change, as can be seen from the differences in octahedral *SHAPE,* Σ and Θ values (Table 4, Table S7). For the Fe(III) SCO complexes studied here, the greater stability of the [LS-HS] state for **3** is therefore also not due to increased intramolecular cooperativity and coupling mediated by $thea^{4-}$ (as shown electrochemically and from computed exchange interactions), as an observable distortion of the other Fe(III) site would be seen upon SCO.

Table 4. Calculated octahedral *SHAPE* parameters for the DFT UOPBE/6-311++G(d,p) optimized gas phase geometry for **1**, **2** and **3** in the [LS-LS], [LS-HS] and [HS-HS] states.

	1 (Fe_1)	**1** (Fe_2)	**2** (Fe_1)	**2** (Fe_2)	**3** (Fe_1)	**3** (Fe_2)
[LS-LS]	0.37[a]	0.37[a]	0.40[a]	0.40[a]	0.36[a]	0.36[a]
[LS-HS]	0.37[a]	1.93[b]	0.40[a]	2.06[b]	0.36[a]	2.00[b]
[HS-HS]	2.03[b]	2.03[b]	2.08[b]	2.08[b]	2.01[b]	2.01[b]

[a] LS-Fe(III) site [b]HS-Fe(III) site. *SHAPE* index for octahedral geometry in SHAPE 2.1.[47,48] A value of 0 represents a perfect octahedron

Instead, the accessibility of a mixed spin-state [LS-HS] intermediate in these bis(catecholate) bridged Fe(III) complexes, as Cirera and Ruiz found for Fe(II) SCO, appears to be most influenced by the ligand field strength. For Fe(III) SCO complexes bridged by a bis(catecholate) ligand, the [LS-HS] stability increases with increasing ligand field following **1** < **2** < **3** (Figure 8). This observation can be extended to the hypothetical complex $[\{Fe^{III}(tpa)\}_2(pip)](PF_6)_2$ ($pipH_4$ = 6,6′-[piperazine-1,4-diyl-bis(methylene)]bis[3,5-di-tert-butyl-pyrocatechol] (Figure S28) calculated previously using DFT UOPBE/6-311++G(d,p).[71] The calculations suggest that pip^{4-} provides an even weaker ligand field compared to $spiro^{4-}$ (due to the electron donating *tert*-butyl groups) (Figure 8), with the [LS-HS] state in this complex destabilized compared to the halfway point between [LS-LS] and [HS-HS], with a ρ of +0.19. It could be envisioned that increasing the ligand field further should stabilize [LS-HS] more, increasing likelihood of experimentally observing two-step SCO in bis(catecholate) Fe(III) dimers.

As mentioned, the increased ligand field strength of Br_4spiro^{4-} compared to $spiro^{4-}$ likely arises from the bromo substituents destabilizing the ligand HOMO orbitals, thereby decreasing the π-donor strength. However, the origin of the difference in ligand field strength between $spiro^{4-}$ and $thea^{4-}$ is less obvious. We suggest that the ligand field strength difference between **1** and **3** reflects the differing extent of electronic communication between the two coordinating catecholate moieties for the different bis(catecholate) ligand classes, as observed by electrochemistry. Calculation of the natural magnetic orbitals of compound **1** in the [LS-LS] state indicates minimal orbital overlap between the two catecholate units in $spiro^{4-}$ through the central spirocyclic carbon (Figure 9). In the case of $thea^{4-}$, even though it is formally non-conjugated system, there is orbital overlap such that the π-system spreads across the two halves of the bridging of the ligand (Figure 9). This larger orbital overlap for $thea^{4-}$ vs $spiro^{4-}$ manifests as increased electronic communication

between the two catecholate groups in each ligand, parameterized from the voltammetry as Δ*diox*. Crucially, this increased orbital overlap extends the π-system to a greater degree in thea^{4-}, which raises the energy of the ligand-centered HOMO and increases the ligand field experienced by the coordinated metal.[89] As well, the larger π-orbital overlap for **3** increases the effectiveness of antiferromagnetic exchange channels, as observed in the larger calculated *J* values for the three spin states in **3** compared to **1** and **2** (Table S5), additionally stabilizing the [LS-LS] state (J = −281 cm^{-1}). The J value of −55 and −6 cm^{-1} for the [LS-HS] and [HS-HS] states for **3**, respectively, are one and two order of magnitude smaller than the values for the [LS-LS] state (Table S5).

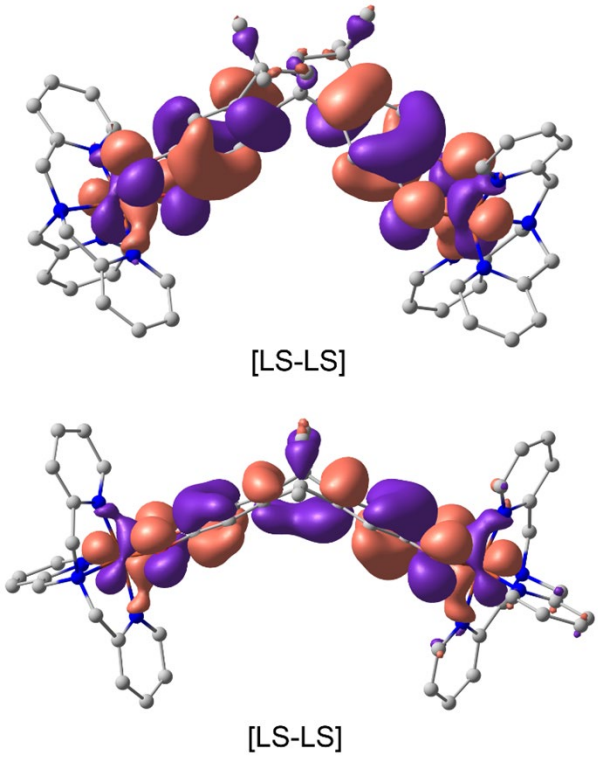

Figure 9. Natural magnetic orbitals in the [LS-LS] states of **1** (top) and **3** (bottom) as calculated by the DFT UOPBE/6-311++G(d,p) method (contour value = 0.017 e/Å^3). The PF_6^- anions are not shown.

CONCLUDING REMARKS

We have reported the synthesis of [{Fe^{III}(tpa)}$_2$spiro](PF$_6$)$_2$ (**1**), [{Fe^{III}(tpa)}$_2$Br$_4$spiro](PF$_6$)$_2$ (**2**), and [{Fe^{III}(tpa)}$_2$thea](PF$_6$)$_2$ (**3**), which form a new family of dinuclear Fe(III) spin crossover complexes, and have characterized their structural, spectroscopic, electrochemical, and magnetic properties. Single crystal X-ray diffraction data for **2**·*i*Pr$_2$O·*x*H$_2$O are consistent with the [HS-HS] state at room temperature. The structure of **3**·Et$_2$O at 100 K appears to contain two dimers in the asymmetric unit adopting a [LS-HS] state. Infrared spectroscopy confirmed a cat^{2-}-cat^{2-} oxidation

state at room temperature for all compounds. Electrochemical measurements indicated two closely spaced cat^{2-}-cat^{2-}/-$SQ^{\bullet-}$ and cat^{2-}-$SQ^{\bullet-}$/ $SQ^{\bullet-}$-$SQ^{\bullet-}$ oxidations and an Fe(III)/Fe(II) reduction. The ligand-based oxidations are at a similar potential for **1** and **3** but shifted higher for **2** because of the bromo substituents. The separation in redox potential between these two closely spaced ligand oxidations indicate similar weak intramolecular electronic communication between the two dioxolene units for **1**, **2** and stronger communication for **3**.

Variable temperature solution UV-Vis and magnetic measurements indicate the onset of SCO for all three compounds from the [HS-HS] state at room temperature upon cooling in several solvents. At 77 K, EPR spectra suggest that **1** and **2** contain a mixture of [LS-LS], [LS-HS] and [HS-HS], and **3** a mixture of [LS-LS] and [LS-HS]. The proportion of [LS-LS] at 77 K increases following **1** < **2** < **3**. In the solid state, variable temperature crystallographic data for **2**·*i*Pr_2O·*x*H_2O are consistent with the onset of a SCO interconversion upon cooling to 30 K, with the Br_4spiro^{4-} remaining in the cat^{2-}-cat^{2-} state. Magnetic susceptibility data for **1**·2H_2O·0.5*i*Pr_2O are consistent with a temperature invariant [HS-HS] state, while **2**·1.3H_2O and **3**·2H_2O·0.5*i*Pr_2O undergo a partial SCO transition, approximated to 33% and 50% conversion to LS-Fe(III).

Density functional theory calculations suggest all three complexes have a [LS-LS] ground state, with the [LS-HS] and [HS-HS] states successively destabilized. The destabilization of the [HS-HS] state follows the order **1** < **2** < **3**, with $thea^{4-}$ providing the strongest ligand field. The calculated energy ordering is reflected qualitatively in the solid-state magnetic data and solution EPR spectra. For all three complexes, the mixed spin [LS-HS] state is stabilized relative to the halfway energy between [LS-LS] and [HS-HS] and increases in the order **1** < **2** < **3**. Therefore, all complexes could be expected to display well-defined mixed spin [LS-HS] state, with **3** the most likely. Due to this relative calculated stability of the [LS-HS] state, the well-defined plateau in the

solid-state magnetic susceptibility data for **3**·2H_2O·0.5*i*Pr_2O at low temperature is assigned to a [LS-HS] state, rather than a mixture of [LS-LS] and [HS-HS]. This is also consistent with the 100 K crystal structure of **3**·Et_2O. For **2**·1.3H_2O, the plateau would therefore most likely arise from a mixture of [LS-HS] and [HS-HS] states.

As understood for dinuclear Fe(II) SCO complexes, the stability of a well-defined mixed spin [LS-HS] state is influenced predominantly by the local electronic environment. For **1**, **2** and **3**, it appears that increasing the ligand field results in increased stability of the [LS-HS] state. The increase in ligand field of Br_4spiro^{4-} compared to spiro^{4-} can be attributed to the bromo groups decreasing the π-donor strength. The stronger ligand field strength of thea^{4-} compared to spiro^{4-} can be explained by the greater π-orbital overlap between the two catecholate units in thea^{4-}, resulting in increased energy of the ligand-based HOMO and reduction in π-donor strength. This increased orbital overlap is also observed from the voltammetry as increased electronic communication in thea^{4-} for **3** compared to spiro^{4-} in **1**. While varying the electron withdrawing/donating character of ligand substituents is typically used to tune ligand field strength, here we have shown that varying the extent of π-orbital overlap can also be used for this purpose and therefore to modulate the characteristics of SCO interconversions.

This work expands both the number of dinuclear Fe(III) SCO compounds and the number of Fe(III) SCO incorporating redox-active ligands. The nature of the SCO interconversion in this family of complexes is directly affected by the bis(catecholatate) ligand, with the ligand field strength modulating the electronic state. This is consistent with the conclusion for dinuclear Fe(II) SCO that the local electronic environment dictates the SCO profile and increasing the ligand field stabilizes the mixed [LS-HS] state. The next step in this story is to explore the redox activity of the bridging bis(catecholate) ligands and the effect on the SCO properties of ligand oxidation.

EXPERIMENTAL SECTION

Synthesis

All manipulations, unless otherwise indicated, were performed under anaerobic conditions in an M-Braun N_2-atmosphere glove box or on a Schlenk line using standard Schlenk techniques. All chemicals purchased were of reagent grade or higher. Reagents Bu_4NPF_6 and ferrocene were purified from hot ethanol recrystallization and sublimation, respectively. Solvents were dried over molecular sieves (3 Å) for a minimum of 3 days and stored under N_2 on sieves until used. Solvents were degassed prior to use via 3 freeze-pump-thaw cycles. Molecular sieves were activated by heating at 300 °C for 48 hours and then cooled under vacuum. Ligands tpa, $Br_4spiroH_4$, and $theaH_4$ were prepared as previously reported.[24,90,91]

[{Fe^{III}(tpa)}$_2$spiro](PF$_6$)$_2$·2H$_2$O·0.5*i*Pr$_2$O (**1**·2H_2O·0.5*i*Pr_2O). A methanolic solution of tpa (0.155 g, 0.53 mmol; 10 mL) was added dropwise to a methanolic solution of $FeCl_3$ (0.086 g, 0.53 mmol; 25 mL), and left to stir for 15 minutes. After, a methanolic solution of $spiroH_4$ (0.091 g, 0.27 mmol; 20 mL), deprotonated with Et_3N (150 µL, 1.1 mmol), was subsequently added resulting in a yellow to dark blue purple change. After stirring for 30 minutes, the solution was filtered to remove the formed solid and combined with a methanolic solution of KPF_6 (0.119 g, 0.65 mmol; 15 mL). The volume of methanol was reduced to create a saturated solution, and then left at −18 °C for 24 hours, after which a microcrystalline powder formed. The solid was collected by vacuum filtration in air, washed with cold methanol and diethyl ether, and air dried to yield **1** as a dark blue solid (0.24 g, 67%). The crude product was recrystallized by layering a filtered MeCN solution of **1** (0.24 g, 8.8 mL) below 20 ml *i*Pr_2O, which after one week, yielded a microcrystalline product (0.18 g, 75%). The sample was collected and washed with *i*Pr_2O, with the crystalline product appearing hygroscopic, analyzing as **1**·2H_2O·0.5*i*Pr_2O. Anal. Calcd for

$C_{60}H_{67}Fe_2N_8O_{6.5}P_2F_{12}$: C, 51.26; H, 4.80; N, 7.97. Found C, 51.55; H, 4.64; N, 7.57. Selected FT-IR data (ATR, cm^{-1}): 2930 (w), 1605 (s), 1449 (m), 1280 (s), 1026 (s), 835 (s), 771 (s), 556 (s). UV-Vis (acetonitrile) λ_{max} (ε): 544 (3850), 924 nm (6350 L mol^{-1} cm^{-1}).

[{Fe^{III}(tpa)}$_2$Br$_4$spiro](PF$_6$)$_2$·1.3H$_2$O (**2**·1.3H_2O). Sample **2** was prepared as per **1**, replacing spiroH_4 with Br$_4$spiroH_4, using tpa (0.086 g, 0.30 mmol), $FeCl_3$ (0.047 g, 0.29 mmol), Br$_4$spiroH_4 (0.097 g, 0.15 mmol), Et_3N (83 μL, 0.6 mmol), and KPF_6 (0.060 g, 0.33 mmol) to give a dark purple microcrystalline solid (0.19 g, 78%). Single crystals suitable for X-ray diffraction were grown from layering a saturated MeCN solution with *i*Pr_2O. The crude product was recrystallized by layering a filtered MeCN solution of **2** (0.18 g, 6 mL) below 18 ml *i*Pr_2O, which after one week, yielded a microcrystalline product (0.12 g, 67%). The sample was collected and washed with *i*Pr_2O, with the crystalline product appearing hygroscopic, analyzing as **2**·1.3H_2O. Anal. Calcd for $C_{57}H_{54.6}Br_4Fe_2N_8O_{5.3}P_2F_{12}$: C, 41.30; H, 3.32; N, 6.76. Found C, 41.52; H, 3.72; N, 7.16. Selected FT-IR data (ATR, cm^{-1}): 2957 (w), 1605 (s), 1447 (m), 1253 (s), 1024 (m), 828 (s), 762 (s), 556 (s). UV-Vis (acetonitrile) λ_{max} (ε): 866 nm (8600 L mol^{-1} cm^{-1}).

[{Fe^{III}(tpa)}$_2$thea](PF$_6$)$_2$·2H$_2$O·0.5*i*Pr$_2$O (**3**·2H_2O·0.5*i*Pr_2O). Sample **3** was prepared as per **1**, replacing spiroH_4 with theaH_4, using tpa (0.249 g, 0.86 mmol), $FeCl_3$ (0.138 g, 0.85 mmol), theaH_4 (0.129 g, 0.43 mmol), Et_3N (240 μL, 1.73 mmol), and KPF_6 (0.161 g, 0.88 mmol) to give a dark purple microcrystalline solid (0.23 g, 55%). The crude product was recrystallized by layering a filtered MeCN solution of **3** (0.23 g, 8.8 mL) below 20 ml *i*Pr_2O, which after one week, yielded a microcrystalline product (0.18 g, 78%). The sample was collected and washed with *i*Pr_2O, with the crystalline product appearing hygroscopic, analyzing as **3**·2H_2O·0.5*i*Pr_2O. Anal. Calcd for $C_{57}H_{61}Fe_2N_8O_{6.5}P_2F_{12}$: C, 50.20; H, 4.51; N, 8.22. Found C, 50.31; H, 4.11; N, 7.86.

Selected FT-IR data (ATR, cm^{-1}): 2930 (w), 1605 (s), 1445 (m), 1284 (s), 1024 (s), 830 (s), 764 (s), 556 (s). UV-Vis (acetonitrile) λ_{max} (ε): 520 (2720), 1020 nm (5660 L mol^{-1} cm^{-1}).

X-ray Data Collection and Structure Solution

Single X-ray diffraction data for **2**·*i*Pr_2O at 30 K were collected using a RigakuOD XtaLAB Synergy-S employing confocal mirror monochromated micro-focus Mo-Kα radiation (λ = 0.731073 Å) with ω and φ scans. Data were integrated, reduced and multi-scan absorption corrections were applied using *CrysAlisPro*.[92] Data for **1**·*i*Pr_2O·*x*H_2O at 100, 150, 200, 250, 300 and 350 K were collected on the MX1[55] beamline at the Australian Synchrotron fitted with a silicon double crystal monochromator, the wavelength being tuned to approximate Mo-Kα radiation (λ = 0.71092 Å) while data for **3**·Et_2O were collected on the MX2[56] beamline at the Australian Synchrotron, the wavelength being tuned to approximate Mo-Kα radiation (λ = 0.71073 Å). Data reduction was performed using XDS, using strong multi-scan absorption correction in SADABS. Crystals were collected at multiple orientations and merged with SADABS.[93] Crystals were transferred directly from the mother liquor to crystallographic oil to prevent solvent loss and loss of crystallinity. Structures were solved with SHELXT[94] and refined using a full matrix least squared procedure based on F^2 using SHELXL within Olex2.[95,96] The solvent molecules in **2**·*i*Pr_2O·*x*H_2O collected at 100, 150, 200, 250, 300 and 350 K were highly disordered, and attempts to satisfactorily model the disorder were unsuccessful. Accordingly, the contribution of the solvent molecules to the structure was treated with the solvent mask routine[97] in Olex2, the composition of the solvent molecules were assigned based on the residual electron density and the volume of the solvent void. All non-hydrogen atoms were refined using anisotropic displacement factors. Hydrogen atoms were placed at geometrical positions and refined using the riding model.

Powder X-ray diffraction (PXRD) data were measured on a Rigaku Synergy Dual Wavelength Rotating Anode X-ray Diffractometer System using Cu-Kα (λ = 1.5418 Å) at 100 K. Powder samples were prepared by crushing the sample gently and loading them into a borosilicate glass capillary for measurement. Data were collected at 2θ = 50° with an exposure time of 60 seconds per frame and processed using CrysAlisPro.

Electronic and Infrared Spectroscopy, Elemental Analysis, Thermogravimetric Analysis

Samples for solution UV-Visible-NIR measurements were prepared in an M-Braun N_2-atmosphere glove box and placed in a gastight cuvette. Solution state UV-Visible-NIR spectra were measured on a PerkinElmer UV-Vis-NIR Spectrometer Lambda 1050. Attenuated total reflectance infrared spectra were measured on a Bruker Alpha spectrometer and normalized as absorbance spectra. Solution State Variable temperature UV-Visible absorption spectra were measured on an Agilent Cary UV-Visible Multicell Peltier Spectrometer, with a flow of N_2 gas to remove condensation. Diffuse reflectance UV-Visible spectra were measured on the samples diluted ~5% in KBr on a Thermo Scientific Evolution 220 UV-Visible spectrophotometer. Elemental analyses (C, H, N) were performed at the Campbell Microanalytical Laboratory, University of Otago. Thermogravimetric analyses were performed on a Mettler Toledo thermal analysis using a ramp rate of 5 °C per minute up to a maximum temperature of 400 °C under an N_2 atmosphere.

Electron Paramagnetic Spectroscopy

The X-band EPR spectra were recorded on a Bruker Magnettech ESR5000. Measurements were performed at room temperature and at 77 K (liquid N_2 temperature) using a cold finger. The 77 K spectra were collected by first freezing the solutions in liquid N_2. The spectra were measured at 9.46 GHz and 10 mW, having confirmed linear power dependence. The measurements were

performed on 40:60 MeCN/toluene (0.1 mM) solutions of **1**, **2** and **3**. Samples were prepared in an M-Braun N_2-atmosphere glove box by first dissolving the solid sample in MeCN, followed by toluene. The solution samples were inspected to make sure no solid precipitate formed upon sitting for one day, as well as upon cooling to 77 K.

Electrochemistry

Samples for electrochemical measurements were prepared in an M-Braun N_2-atmosphere glove box. Electrochemical measurements were performed in MeCN at room temperature using a standard three-electrode configuration connected to an eDAQ computer-controlled potentiostat. Measurements were performed under a constant flow of N_2. For cyclic voltammetry measurements, the three-electrode system consisted of a 1.0 mm diameter glassy carbon electrode (Cypress Systems), a platinum/titanium auxiliary electrode (eDAQ), and a Ag/AgCl reference electrode (eDAQ). For steady state voltammetry measurements, the working electrode was replaced with a 3.0 mm diameter glassy carbon rotating disk electrode with external controller (Metrohm). Analyte solutions of 1.0 mM were prepared using anaerobic techniques in 5 ml MeCN containing 0.25 M Bu_4NPF_6 as the supporting electrolyte. All potentials have been references *versus* the ferrocene/ferrocenium redox couple, measured immediately afterwards. The cyclic voltammetry (CV) midpoint potentials (E_m) are calculated by taking the average of the anodic and cathodic peak potentials (Ep). The half-wave potentials ($E_{1/2}$) are calculated as the potential at half the limiting current (i_L). Reversible processes are identified by peak-to-peak separations (ΔE_p) close to the value measured under the same conditions for ferrocene at a scan rate of 100 mV s^{-1} (68–81 mV in MeCN).

Solution-Based Magnetic Measurements

Solution-based magnetic susceptibility measurements were measured in MeCN (238 – 318 K) by ^{1}H NMR spectroscopy according to Evans method.[64] Measurements were recorded on a Bruker Av500 NMR spectrometer equipped with a 5 mm TCI CryoProbe Prodigy ^{1}H/^{2}H-^{13}C-^{15}N probe. Cooling was achieved with a Bruker BCU-II gas pre-conditioner. Sample temperature was calibrated using d_4-methanol and stable at ±0.1 K. The solution samples were prepared in an M-Braun N_2-atmosphere glove box and measured in an anaerobic NMR tube equipped with a J Young tap. A solvent mixture was prepared containing d_3-MeCN and 0.5 – 2% H_3-MeCN as a standard. The compound was dissolved in the solvent mixture under anaerobic conditions to form a solution of precisely known concentration and placed inside an NMR tube with an attached J-Young valve. A narrow capillary was filled with the same solvent mixture and placed inside the NMR tube as an internal reference. The shift in the H_3-MeCN singlet in the paramagnetic solution compared to H_3-MeCN in the internal references, Δυ in hertz, can be used to calculate the mass susceptibility of the compound, χ_g, according to eq 1.

$$\chi_g = \frac{3\Delta\upsilon}{4\pi m\upsilon} + \chi_0 + \chi_0 \frac{d_0 - d_s}{m} \quad (1)$$

where m is the concentration of the paramagnetic solution (in g cm^{-3}), corrected for the temperature dependence of the density of the solvent,[98,99] υ is the spectrometer frequency (in Hz), χ_0 is the mass susceptibility of the solvent mixture, d_0 is the density of the pure solvent mixture, and d_s is the density of the compound solution. As the sample solution is dilute, the following approximation can be made: $d_s = d_s + m$, leading to a cancelation of the second and third terms of eq. 1. The mass susceptibility is converted to the molar susceptibility by multiplying by the molecular weight (including molecules of solvation) and then corrected for the diamagnetic contribution of the compound using Pascal's constants.[100]

Solid-State Magnetic Measurements

The dc susceptibility and magnetization measurements for samples **1**·2H_2O·0.5*i*Pr_2O, **2**·1.3H_2O and **3**·2H_2O·0.5*i*Pr_2O were performed on a Quantum Design MPMS 3 SQUID magnetometer measured between 1.8 and 300 K with an applied field of 1000 Oe. Measurements employed scan rates of 2 K/min for 20–300 K, 1 K/min for 10–19 K, and 0.5 K/min for 1.8–9 K. The data was corrected for the diamagnetic contribution of the gel cap, and of the sample using Pascal's constants.[100] Each sample was measured from 300 to 1.8 K, before measuring back to 300 K. Magnetization (M) vs field (H) measurements were performed between 0 and 7 T at 1.8, 4 and 7 K. Fitting the magnetic data made use of the program PHI.[59]

Density Functional Theory (DFT) Calculations

The DFT calculations were performed using the Gaussian 16[68] program package with the UOPBE[69,70] functional and the 6-311++G(d,p) basis set including diffuse and polarization functions at all atoms. The stationary points on the potential energy surfaces (PESs) were localized by a full geometry optimization, with subsequent confirmation of the stabilities of the DFT wave function. Belonging the found stationary points to the minima on the PESs were determined by calculating the force constant matrices. The solvent effects were accounted for by using the SMD continuum solvation with acetonitrile as solvent. [67] The estimation of the exchange spin coupling J (in cm^{-1}; $= -2JS_1 \cdot S_2$) was carried out by means of calculation of all possible charge distributions in the framework of 'broken symmetry' (BS) formalism with the use of Yamaguchi equation.[81,101] Structural visualizations were prepared using the ChemCraft[102] software with the calculated atomic coordinates as input parameters.

ASSOCIATED CONTENT

Supporting Information

The Supporting Information is available free of charge at X.

Additional TGA, powder X-ray diffraction, crystallographic and structural data, structural analysis, IR, magnetic measurements, UV-Vis-NIR, and DFT (PDF)

DFT optimized XYZ coordinates of complexes (ZIP)

Accession Codes

CCDC 2256687-2256694 contains the supplementary crystallographic data for this paper. These data can be obtained free of charge via www.ccdc.cam.ac.uk/data_request/cif, or by emailing data_request@ccdc.cam.ac.uk, or by contacting The Cambridge Crystallographic Data Centre, 12 Union Road, Cambridge CB2 1EZ, UK; fax: +44 1223 336033.

AUTHOR INFORMATION

Corresponding Author

Colette Boskovic − School of Chemistry, University of Melbourne, Victoria 3010, Australia; orcid.org/0000- 0002-1882-2139; Email: c.boskovic@unimelb.edu.au

Author Contributions

The manuscript was written through contributions of all authors. All authors have given approval to the final version of the manuscript.

Notes

The authors declare no competing financial interest.

ACKNOWLEDGMENT

C.B. and J.K.C. thank the Australian Research Council for funding (FT190100293; LE170100144). J.T.J acknowledges support from the Australian Government for a Research Training Stipend. M.G.C. and A.A.S. thank the Ministry of Science and Higher Education of the Russian Federation (State assignment in the field of scientific activity, project No. FENW-2023-0017). G.K.G. acknowledges support from the European Research Council (CoG-816268), awarded to Prof. David Mills. This work was performed in part at the Trace Analysis for Chemical, Earth and Environmental Sciences (TrACEES) Platform at the University of Melbourne. This research was undertaken in part using the MX1 and MX2 beamlines at the Australian Synchrotron, part of ANSTO, Victoria, Australia and made use of the Australian Cancer Research Foundation (ACRF) detectors (for MX2). We acknowledge the Australian Research Council for an equipment grant (LE210100009 and LE230100048). We acknowledge the EPSRC UK National Electron Paramagnetic Resonance Service for access to the SQUID magnetometer (EP/S033181/1).

REFERENCES

(1) Gütlich, P.; Goodwin, H. A. *Spin Crossover in Transition Metal Compounds III*; Springer., 2004

(2) Real, J. A.; Gaspar, A. B.; Carmen Muñoz, M. Thermal, Pressure and Light Switchable Spin-Crossover Materials. *Dalton Transactions* **2005**, 2062–2079.

(3) Halcrow, M. A. *Spin-Crossover Materials: Properties and Applications*; John Wiley & Sons Ltd., 2013.

(4) Lefter, C.; Davesne, V.; Salmon, L.; Molnár, G.; Demont, P.; Rotaru, A.; Bousseksou, A. Charge Transport and Electrical Properties of Spin Crossover Materials: Towards Nanoelectronic and Spintronic Devices. *Magnetochemistry* **2016**, *2*, 18.

(5) Khusniyarov, M. M. How to Switch Spin-Crossover Metal Complexes at Constant Room Temperature. *Chemistry - A European Journal* **2016**, *22*, 15178–15191.

(6) Senthil Kumar, K.; Ruben, M. Emerging Trends in Spin Crossover (SCO) Based Functional Materials and Devices. *Coord. Chem. Rev.* **2017**, *346*, 176–205.

(7) Hogue, R. W.; Singh, S.; Brooker, S. Spin Crossover in Discrete Polynuclear Iron(II) Complexes. *Chem. Soc. Rev.* **2018**, *47*, 7303–7338.

(8) Senthil Kumar, K.; Bayeh, Y.; Gebretsadik, T.; Elemo, F.; Gebrezgiabher, M.; Thomas, M.; Ruben, M. Spin-Crossover in Iron(II)-Schiff Base Complexes. *Dalton Transactions* **2019**, *48*, 15321–15337.

(9) Brooker, S. Spin Crossover with Thermal Hysteresis: Practicalities and Lessons Learnt. *Chem. Soc. Rev.* **2015**, *44*, 2880–2892.

(10) Villalva, J.; Develioglu, A.; Montenegro-Pohlhammer, N.; Sánchez-de-Armas, R.; Gamonal, A.; Rial, E.; García-Hernández, M.; Ruiz-Gonzalez, L.; Costa, J. S.; Calzado, C. J.; Pérez, E. M.; Burzurí, E. Spin-State-Dependent Electrical Conductivity in Single-Walled Carbon Nanotubes Encapsulating Spin-Crossover Molecules. *Nat. Commun.* **2021**, *12*, 1–8.

(11) Seo, J.; Braun, J. D.; Dev, V. M.; Mason, J. A. Driving Barocaloric Effects in a Molecular Spin-Crossover Complex at Low Pressures. *J. Am. Chem. Soc.* **2022**, *144*, 6493–6503.

(12) Valverde-Muñoz, F. J.; Seredyuk, M.; Muñoz, M. C.; Molnár, G.; Bibik, Y. S.; Real, J. A. Thermochromic Meltable Materials with Reverse Spin Transition Controlled by Chemical Design. *Angew. Chem., Int. Ed. 2007,***2020**, *59*, 18632–18638.

(13) Torres-Cavanillas, R.; Morant-Giner, M.; Escorcia-Ariza, G.; Dugay, J.; Canet-Ferrer, J.; Tatay, S.; Cardona-Serra, S.; Giménez-Marqués, M.; Galbiati, M.; Forment-Aliaga, A.; Coronado, E. Spin-Crossover Nanoparticles Anchored on MoS_2 Layers for Heterostructures with Tunable Strain Driven by Thermal or Light-Induced Spin Switching. *Nat. Chem.* **2021**, *13*, 1101–1109.

(14) Kipgen, L.; Bernien, M.; Tuczek, F.; Kuch, W. Spin-Crossover Molecules on Surfaces: From Isolated Molecules to Ultrathin Films. *Advanced Materials* **2021**, *33*, 2008141.

(15) Harding, D. J.; Harding, P.; Phonsri, W. Spin Crossover in Iron(III) Complexes. *Coord. Chem. Rev.* **2016**, *313*, 38–61.

(16) Karuppannan, S. K.; Martín-Rodríguez, A.; Ruiz, E.; Harding, P.; Harding, D. J.; Yu, X.; Tadich, A.; Cowie, B.; Qi, D.; Nijhuis, C. A. Room Temperature Conductance Switching in a Molecular Iron(III) Spin Crossover Junction. *Chem. Sci.* **2021**, *12*, 2381–2388.

(17) Martinho, P. N.; Lemma, T.; Gildea, B.; Picardi, G.; Müller-Bunz, H.; Forster, R. J.; Keyes, T. E.; Redmond, G.; Morgan, G. G. Template Assembly of Spin Crossover One-Dimensional Nanowires. *Angew. Chem., Int. Ed. 2007,***2012**, *51*, 11995–11999.

(18) Gandolfi, C.; Moitzi, C.; Schurtenberger, P.; Morgan, G. G.; Albrecht, M. Improved Cooperativity of Spin-Labile Iron(III) Centers by Self-Assembly in Solution. *J. Am. Chem. Soc.* **2008**, *130*, 14434–14435.

(19) Boonprab, T.; Lee, S. J.; Telfer, S. G.; Murray, K. S.; Phonsri, W.; Chastanet, G.; Collet, E.; Trzop, E.; Jameson, G. N. L.; Harding, P.; Harding, D. J. The First Observation of Hidden Hysteresis in an Iron(III) Spin-Crossover Complex. *Angew. Chem., Int. Ed. 2007,***2019**, *58*, 11811–11815.

(20) Simaan, A. J.; Boillot, M. L.; Rivière, E.; Boussac, A.; Girerd, J. J. A Two-Step Spin Crossover in [(TPA)Fe(III)(Cat)]BPh_4. *Angew. Chem., Int. Ed. 2007,***2000**, *39*, 196–198.

(21) Real, J. A.; Bolvin, H.; Bousseksou, A.; Dworkin, A.; Kahn, O.; Varret, F.; Zarembowitch, J. Two-Step Spin Crossover in the New Dinuclear Compound $[Fe(Bt)(NCS)_2]_2$bpym, with Bt = 2,2′-Bi-2-Thiazoline and Bpym = 2,2′-Bipyrimidine: Experimental Investigation and Theoretical Approach. *J. Am. Chem. Soc.* **1992**, *114*, 4650–4658.

(22) Verat, A. Y.; Ould-Moussa, N.; Jeanneau, E.; Guennic, B. Le; Bousseksou, A.; Borshch, S. A.; Matouzenko, G. S. Ligand Strain and the Nature of Spin Crossover in Binuclear Complexes: Two-Step Spin Crossover in a 4,4'-Bipyridine-Bridged Iron(II) Complex $[\{Fe(Dpia)(NCS)_2\}_2$(4,4'-Bpy)] (Dpia = Di(2-Picolyl)Amine; 4,4-Bpy = 4,4'bipyridine). *Chemistry - A European Journal* **2009**, *15*, 10070–10082.

(23) Fujinami, T.; Nishi, K.; Kitashima, R.; Murakami, K.; Matsumoto, N.; Iijima, S.; Toriumi, K. One-Step and Two-Step Spin Crossover Binuclear Iron(III) Complexes Bridged by 4,4′-Bipyridine. *Inorganica Chim. Acta* **2011**, *376*, 136–143.

(24) Gransbury, G. K.; Livesay, B. N.; Janetzki, J. T.; Hay, M. A.; Gable, R. W.; Shores, M. P.; Starikova, A.; Boskovic, C. Understanding the Origin of One- or Two-Step Valence Tautomeric Transitions in Bis(Dioxolene)-Bridged Dinuclear Cobalt Complexes. *J. Am. Chem. Soc.* **2020**, *142*, 10692–10704.

(25) Singh, S.; Brooker, S. Correlations between Ligand Field Δ_O, Spin Crossover $T_{1/2}$ and Redox Potential E_{Pa} in a Family of Five Dinuclear Helicates . *Chem. Sci.* **2021**, *24*, 30–35.

(26) Ksenofontov, V.; Gaspar, A. B.; Niel, V.; Reiman, S.; Real, J. A.; Gütlich, P. On the Nature of the Plateau in Two-Step Dinuclear Spin-Crossover Complexes. *Chemistry - A European Journal* **2004**, *10*, 1291–1298.

(27) Real, J. A.; Castro, I.; Bousseksou, A.; Verdaguer, M.; Burriel, R.; Castro, M.; Linares, J.; Varret, F. Spin Crossover in the 2,2′-Bipyrimidine-(Bpym-) Bridged Iron(II) Complexes $[Fe(L)(NCX)_2]_2$(Bpym) (L = 2, 2′-Bithiazoline (Bt) and Bpym; X = S, Se). X-Ray Absorption Spectroscopy, Magnetic Susceptibility, Calorimetric, and Mössbauer Spectroscopy Studies. *Inorg. Chem.* **1997**, *36*, 455–464.

(28) Matouzenko, G. S.; Jeanneau, E.; Yu. Verat, A.; Bousseksou, A. Spin Crossover and Polymorphism in a Family of 1,2-Bis(4-Pyridyl)Ethene-Bridged Binuclear Iron(II) Complexes. A Key Role of Structural Distortions. *Dalton Transactions* **2011**, *40*, 9608–9618.

(29) Cirera, J.; Ruiz, E. Theoretical Modeling of Two-Step Spin-Crossover Transitions in Fe^{II} Dinuclear Systems. *J. Mater. Chem. C* **2015**, *3*, 7954–7961.

(30) Kitashima, R.; Imatomi, S.; Yamada, M.; Matsumoto, N.; Maeda, Y. Gradual Two-Step Spin Crossover Behavior of Binuclear Iron(III) Complex Bridged by Trans-1,2-Bis(4-Pyridyl)Ethylene. *Chem. Lett.* **2005**, *34*, 1388–1389.

(31) Imatomi, S.; Sato, T.; Hamamatsu, T.; Kitashima, R.; Matsumoto, N. Spin-Crossover Behavior of Isomorphous Bi- And Mononuclear Iron(III) Complexes. *Bull. Chem. Soc. Jpn.* **2007**, *80*, 2375–2377.

(32) Nemec, I.; Boča, R.; Herchel, R.; Trávníček, Z.; Gembický, M.; Linert, W. Dinuclear Fe(III) Complexes with Spin Crossover. *Monatsh. Chem.* **2009**, *140*, 815–828.

(33) Floquet, S.; Simaan, A. J.; Rivière, E.; Nierlich, M.; Thuéry, P.; Ensling, J.; Gütlich, P.; Girerd, J.-J.; Boillot, M.-L. Spin Crossover of Ferric Complexes with Catecholate Derivatives. Single-Crystal X-Ray Structure, Magnetic and Mössbauer Investigations. *Dalton Transactions* **2005**, 1734–1742.

(34) Tichnell, C. R.; Shultz, D. A.; Popescu, C. V.; Sokirniy, I.; Boyle, P. D. Synthesis, Characterization, and Photophysical Studies of an Iron(III) Catecholate-Nitronylnitroxide Spin-Crossover Complex. *Inorg. Chem.* **2015**, *54*, 4466–4474.

(35) Tezgerevska, T.; Rousset, E.; Gable, R. W.; Jameson, G. N. L.; Sañudo, E. C.; Starikova, A.; Boskovic, C. Valence Tautomerism and Spin Crossover in Pyridinophane–Cobalt–Dioxolene Complexes: An Experimental and Computational Study. *Dalton Transactions* **2019**, *48*, 11674–11689.

(36) Yu, F.; Zhang, Y. M.; Li, A. H.; Li, B. A Spin-Crossover Catecholato-Iron(III) System: Synthesis, Crystal Structure and Magnetic Properties. *Inorg. Chem. Commun.* **2015**, *51*, 87–89.

(37) Tissot, A.; Shepherd, H. J.; Toupet, L.; Collet, E.; Sainton, J.; Molnár, G.; Guionneau, P.; Boillot, M. Temperature- and Pressure-Induced Switching of the Molecular Spin State of an Orthorhombic Iron(III) Spin-Crossover Salt. *Eur. J. Inorg. Chem.* **2013**, *2013*, 1001–1008.

(38) Girerd, J. J.; Boillot, M. L.; Blain, G.; Rivière, E. An EPR Investigation of the Electronic Structure of Pseudo-Octahedral and Spin Crossover Catecholato-Iron(III) Complexes in the Low-Spin State. *Inorganica Chim. Acta* **2008**, *361*, 4012–4016.

(39) Higuchi, M.; Hitomi, Y.; Minami, H.; Tanaka, T.; Funabiki, T. Correlation of Spin States and Spin Delocalization with the Dioxygen Reactivity of Catecholatoiron(III) Complexes. *Inorg. Chem.* **2005**, *44*, 8810–8821.

(40) Hitomi, Y.; Higuchi, M.; Minami, H.; Tanaka, T.; Funabiki, T. Tuning of Spin Crossover Equilibrium in Catecholatoiron(III) Complexes by Supporting Ligands. *Chemical Communications* **2005**, 1758.

(41) Simaan, A. J.; Boillot, M.-L.; Carrasco, R.; Cano, J.; Girerd, J.-J.; Mattioli, T. A.; Ensling, J.; Spiering, H.; Gütlich, P. Electronic, Vibrational, and Structural Properties of a Spin-Crossover Catecholato-Iron System in the Solid State: Theoretical Study of the Electronic

Nature of the Doublet and Sextet States. *Chemistry - A European Journal* **2005**, *1*, 1779–1793.

(42) Hitomi, Y.; Yoshida, M.; Higuchi, M.; Minami, H.; Tanaka, T.; Funabiki, T. A Linear Correlation between Energy of LMCT Band and Oxygenation Reaction Rate of a Series of Catecholatoiron(III) Complexes: Initial Oxygen Binding during Intradiol Catechol Oxygenation. *J. Inorg. Biochem.* **2005**, *99*, 755–763.

(43) Chegerev, M.; Demidov, O.; Vasilyev, P.; Efimov, N.; Kubrin, S.; Starikov, A.; Vlasenko, V.; Piskunov, A.; Shapovalova, S.; Guda, A.; Rusalev, Y.; Soldatov, A. Spin Transitions in Ferric Catecholate Complexes Mediated by Outer-Sphere Counteranions. *Dalton Transactions* **2022**, *51*, 10909–10919.

(44) Alley, K. G.; Poneti, G.; Robinson, P. S. D.; Nafady, A.; Moubaraki, B.; Aitken, J. B.; Drew, S. C.; Ritchie, C.; Abrahams, B. F.; Hocking, R. K.; Murray, K. S.; Bond, A. M.; Harris, H. H.; Sorace, L.; Boskovic, C. Redox Activity and Two-Step Valence Tautomerism in a Family of Dinuclear Cobalt Complexes with a Spiroconjugated Bis(Dioxolene) Ligand. *J. Am. Chem. Soc.* **2013**, *135*, 8304–8323.

(45) Poneti, G.; Mannini, M.; Cortigiani, B.; Poggini, L.; Sorace, L.; Otero, E.; Sainctavit, P.; Sessoli, R.; Dei, A. Magnetic and Spectroscopic Investigation of Thermally and Optically Driven Valence Tautomerism in Thioether-Bridged Dinuclear Cobalt-Dioxolene Complexes. *Inorg. Chem.* **2013**, *52*, 11798–11805.

(46) Fürmeyer, F.; Carrella, L. M.; Ksenofontov, V.; Möller, A.; Rentschler, E. Phase Trapping in Multistep Spin Crossover Compound. *Inorg. Chem.* **2020**, *59*, 2843–2852.

(47) Llunell, M.; Casanova, D.; Cirera, J.; Alemany, P.; Alvarez, S. *SHAPE, 2.1*; Universitat de Barcelona: Barecelona, Spain, 2013.

(48) Alvarez, S.; Avnir, D.; Llunell, M.; Pinsky, M. Continuous Symmetry Maps and Shape Classification. The Case of Six-Coordinated Metal Compounds. *New Journal of Chemistry* **2002**, *26*, 996–1009.

(49) Ketkaew, R.; Tantirungrotechai, Y.; Harding, P.; Chastanet, G.; Guionneau, P.; Marchivie, M.; Harding, D. J. OctaDist: A Tool for Calculating Distortion Parameters in Spin Crossover and Coordination Complexes. *Dalton Transactions* **2021**, *50*, 1086–1096.

(50) Collet, E.; Boillot, M. L.; Hebert, J.; Moisan, N.; Servol, M.; Lorenc, M.; Toupet, L.; Buron-Le Cointe, M.; Tissot, A.; Sainton, J. Polymorphism in the Spin-Crossover Ferric Complexes $[(TPA)Fe^{III}(TCC)]PF_6$. *Acta Crystallogr., Section B* **2009**, *65*, 474–480.

(51) Thorarinsdottir, A. E.; Bjornsson, R.; David Harris, T. Insensitivity of Magnetic Coupling to Ligand Substitution in a Series of Tetraoxolene Radical-Bridged Fe_2 Complexes. *Inorg. Chem.* **2020**, *59*, 4634–4649.

(52) Min, K. S.; Swierczek, K.; DiPasquale, A. G.; Rheingold, A. L.; Reiff, W. M.; Arif, A. M.; Miller, J. S. A Dinuclear Iron(II) Complex, $[(TPyA)Fe^{II}(THBQ^{2-})FeII(TPyA)](BF_4)_2$ [TPyA = Tris(2-Pyridylmethyl)Amine; $THBQ^{2-}$ = 2,3,5,6-Tetrahydroxy-1,4-

Benzoquinonate] Exhibiting Both Spin Crossover with Hysteresis and Ferromagnetic Exchange. *Chemical Communications* **2008**, *22*, 317–319.

(53) Brown, S. N. Metrical Oxidation States of 2-Amidophenoxide and Catecholate Ligands: Structural Signatures of Metal–Ligand π Bonding in Potentially Noninnocent Ligands. *Inorg. Chem.* **2012**, *51*, 1251–1260.

(54) Carugo, O.; Castellani, C. B.; Djinovic, K.; Rizzi, M. Ligands Derived from O-Benzoquinone: Statistical Correlation between Oxidation State and Structural Features. *Dalton Transactions* **1992**, 837–841.

(55) Cowieson, N. P.; Aragao, D.; Clift, M.; Ericsson, D. J.; Gee, C.; Harrop, S. J.; Mudie, N.; Panjikar, S.; Price, J. R.; Riboldi-Tunnicliffe, A.; Williamson, R.; Caradoc-Davies, T. MX1: A Bending-Magnet Crystallography Beamline Serving Both Chemical and Macromolecular Crystallography Communities at the Australian Synchrotron. *J. Synchrotron. Radiat.* **2015**, *22*, 187–190.

(56) Aragão, D.; Aishima, J.; Cherukuvada, H.; Clarken, R.; Clift, M.; Cowieson, N. P.; Ericsson, D. J.; Gee, C. L.; Macedo, S.; Mudie, N.; Panjikar, S.; Price, J. R.; Riboldi-Tunnicliffe, A.; Rostan, R.; Williamson, R.; Caradoc-Davies, T. T. MX2: A High-Flux Undulator Microfocus Beamline Serving Both the Chemical and Macromolecular Crystallography Communities at the Australian Synchrotron. *J Synchrotron Radiat* **2018**, *25*, 885–891.

(57) Tourón Touceda, P.; Mosquera Vázquez, S.; Lima, M.; Lapini, A.; Paolo, F.; Andrea, D.; Roberto, R. Transient Infrared Spectroscopy: A New Approach to Investigate Valence Tautomerism. *Physical Chemistry Chemical Physics* **2012**, *14*, 1038–1047.

(58) Rupp, F.; Chevalier, K.; Graf, M.; Schmitz, M.; Kelm, H.; Grün, A.; Zimmer, M.; Gerhards, M.; van Wüllen, C.; Krüger, H.-J.; Diller, R. Spectroscopic, Structural, and Kinetic Investigation of the Ultrafast Spin Crossover in an Unusual Cobalt(II) Semiquinonate Radical Complex. *Chemistry - A European Journal* **2017**, *23*, 2119–2132.

(59) Chilton, N. F.; Anderson, R. P.; Turner, L. D.; Soncini, A.; Murray, K. S. PHI: A Powerful New Program for the Analysis of Anisotropic Monomeric and Exchange-Coupled Polynuclear d- and f-Block Complexes. *J. Comput. Chem.* **2013**, *34*, 1164–1175.

(60) Nakano, K.; Kawata, S.; Yoneda, K.; Fuyuhiro, A.; Yagi, T.; Nasu, S.; Morimoto, S.; Kaizaki, S. Direct Two-Step Spin-Crossover through [HS-HS]···[LS-LS] at the Plateau in Dinuclear Diiron(II) Complex $[\{Fe(NCBH_3)(4phpy)\}_2(\mu\text{-Bpypz})_2]$. *Chemical Communications* **2004**, *2*, 2892–2893..

(61) Cox, D. D.; Benkovic, S. J.; Bloom, L. M.; Bradley, F. C.; Nelson, M. J.; Que, L.; Wallick, D. E. Catecholate LMCT Bands as Probes for the Active Sites of Nonheme Iron Oxygenases. *J. Am. Chem. Soc.* **1988**, *110*, 2026–2032.

(62) Wu, S.-Q.; Liu, M.; Gao, K.; Kanegawa, S.; Horie, Y.; Aoyama, G.; Okajima, H.; Sakamoto, A.; Baker, M. L.; Huzan, M. S.; Bencok, P.; Abe, T.; Shiota, Y.; Yoshizawa, K.;

Xu, W.; Kou, H.-Z.; Sato, O. Macroscopic Polarization Change via Electron Transfer in a Valence Tautomeric Cobalt Complex. *Nat. Commun.* **2020**, *11*, 1992.

(63) Enachescu, C.; Hauser, A.; Girerd, J. J.; Boillot, M. L. Photoexcitation and Relaxation Dynamics of Catecholato-Iron(III) Spin-Crossover Complexes. *ChemPhysChem* **2006**, *7*, 1127–1135.

(64) Evans, D. F. The Determination of the Paramagnetic Susceptibility of Substances in Solution by Nuclear Magnetic Resonance. *Journal of the Chemical Society* **1959**, 2003.

(65) Loughrey, J. J.; Sproules, S.; McInnes, E. J. L.; Hardie, M. J.; Halcrow, M. A. Stable Mixed-Valent Radicals from Platinum(II) Complexes of a Bis(Dioxolene) Ligand. *Chemistry - A European Journal* **2014**, *20*, 6272–6276.

(66) D'alessandro, D. M.; Keene, F. R. Current Trends and Future Challenges in the Experimental, Theoretical and Computational Analysis of Intervalence Charge Transfer (IVCT) Transitions. *Chem. Soc. Rev.* **2006**, *35*, 424–440.

(67) Marenich, A. V.; Cramer, C. J.; Truhlar, D. G. Universal Solvation Model Based on Solute Electron Density and on a Continuum Model of the Solvent Defined by the Bulk Dielectric Constant and Atomic Surface Tensions. *Journal of Physical Chemistry B* **2009**, *113*, 6378–6396.

(68) Frisch, M. J.; Trucks, G. W.; Schlegel, H. B.; Scuseria, G. E.; Robb, M. A.; Cheeseman, J. R.; Scalmani, G.; Barone, V.; Petersson, G. A.; Nakatsuji, H.; Li, X.; Caricato, M.; Marenich, A. V.; Bloino, J.; Janesko, B. G.; Gomperts, R.; Mennucci, B.; Hratch, D. J. et al., *Gaussian 16*, revision C.01.

(69) Swart, M.; Ehlers, A. W.; Lammertsma, K. Performance of the OPBE Exchange-Correlation Functional. *Mol. Phys.* **2004**, *102*, 2467–2474.

(70) Swart, M.; Groenhof, A. R.; Ehlers, A. W.; Lammertsma, K. Validation of Exchange-Correlation Functional for Spin States of Iron Complexes. *Journal of Physical Chemistry A* **2004**, *108*, 5479–5483.

(71) Chegerev, M. G.; Starikova, A. A. A Computational Search for Spin-Crossover in Bis(Catecholate) Diiron Complexes. *Comput. Theor. Chem.* **2022**, *1211*, 113693.

(72) Starikova, A. A.; Chegerev, M. G.; Starikov, A. G. Computational Modeling of Structure and Magnetic Properties of Dinuclear Di-o-Benzoquinone Iron Complexes with Linear Polycyclic Linkers. *Russian Chemical Bulletin* **2020**, *69*, 203–211.

(73) Hay, M. A.; Janetzki, J. T.; Kumar, V. J.; Gable, R. W.; Clérac, R.; Starikova, A. A.; Low, P. J.; Boskovic, C. Modulation of Charge Distribution in Cobalt-α-Diimine Complexes toward Valence Tautomerism. *Inorg. Chem.* **2022**, *61*, 17609–17622.

(74) Cirera, J.; Via-Nadal, M.; Ruiz, E. Benchmarking Density Functional Methods for Calculation of State Energies of First Row Spin-Crossover Molecules. *Inorg. Chem.* **2018**, *57*, 14097–14105.

(75) Siig, O. S.; Kepp, K. P. Iron(II) and Iron(III) Spin Crossover: Toward an Optimal Density Functional. *Journal of Physical Chemistry A* **2018**, *122*, 4208–4217.

(76) Sirirak, J.; Sertphon, D.; Phonsri, W.; Harding, P.; Harding, D. J. Comparison of Density Functionals for the Study of the High Spin Low Spin Gap in Fe(III) Spin Crossover Complexes. *Int. J. Quantum Chem.* **2017**, *117*, 1–8.

(77) Swart, M. Accurate Spin-State Energies for Iron Complexes. *J. Chem. Theory Comput.* **2008**, *4*, 2057–2066.

(78) Starikova, A. A.; Chegerev, M. G.; Starikov, A. G.; Minkin, V. I. A DFT Computational Study of the Magnetic Behaviour of Cobalt Dioxolene Complexes of Tetraazamacrocyclic Ligands. *Comput. Theor. Chem.* **2018**, *1124*, 15–22.

(79) Minkin, V. I.; Starikov, A. G.; Starikova, A. A. Computational Insight into Magnetic Behavior and Properties of the Transition Metal Complexes with Redox-Active Ligands: A DFT Approach. *Pure and Applied Chemistry* **2018**, *90* (5), 811–824.

(80) Starikova, A. A.; Chegerev, M. G.; Starikov, A. G. Computational Insight into Magnetic Behaviour of Cobalt Tris(2-Pyridylmethyl)Amine Complexes with Dioxolenes Incorporating Stable Radicals. *Chem. Phys. Lett.* **2021**, *762*, 138128.

(81) Noodleman, L. Valence Bond Description of Antiferromagnetic Coupling in Transition Metal Dimers. *J. Chem. Phys.* **1981**, *74*, 5737–5743.

(82) Cramer, C. J.; Truhlar, D. G. Density Functional Theory for Transition Metals and Transition Metal Chemistry. *Physical Chemistry Chemical Physics* **2009**, *11*, 10757–10816.

(83) Phillips, J. J.; Peralta, J. E. Towards the Blackbox Computation of Magnetic Exchange Coupling Parameters in Polynuclear Transition-Metal Complexes: Theory, Implementation, and Application. *Journal of Chemical Physics* **2013**, *138*, 174115.

(84) Weissman, S.; Antkowiak, M.; Brzostowski, B.; Kamieniarz, G.; Kronik, L. Accurate Magnetic Couplings in Chromium-Based Molecular Rings from Broken-Symmetry Calculations within Density Functional Theory. *J. Chem. Theory Comput.* **2019**, *15*, 4885–4895.

(85) Fitzhugh, H. C.; Furness, J. W.; Pederson, M. R.; Peralta, J. E.; Sun, J. Comparative Density Functional Theory Study of Magnetic Exchange Coupling in Di-Nuclear Transition Metal Complexes. **2023**, 1–12.

(86) Joshi, R. P.; Phillips, J. J.; Mitchell, K. J.; Christou, G.; Jackson, K. A.; Peralta, J. E. Accuracy of Density Functional Theory Methods for the Calculation of Magnetic Exchange Couplings in Binuclear Iron(III) Complexes. *Polyhedron* **2020**, *176*, 114194.

(87) Starikova, A. A.; Minkin, V. I. Adducts of Transition Metal Complexes with Redox-Active Ligands: The Structure and Spin-State-Switching Rearrangements. *Russian Chemical Reviews* **2018**, *87*, 1049–1079.

(88) Zein, S.; Borshch, S. A. Energetics of Binuclear Spin Transition Complexes. *J. Am. Chem. Soc.* **2005**, *127*, 16197–16201.

(89) Janetzki, J. T.; Zahir, F. Z. M.; Gable, R. W.; Phonsri, W.; Murray, K. S.; Goerigk, L.; Boskovic, C. A Convenient DFT-Based Strategy for Predicting Transition Temperatures of Valence Tautomeric Molecular Switches. *Inorg. Chem.* **2021**, *60*, 14475–14487.

(90) Molteni, V.; Rhodes, D.; Rubins, K.; Hansen, M.; Bushman, F. D.; Siegel, J. S. A New Class of HIV-1 Integrase Inhibitors: The 3,3,3',3'-Tetramethyl-1,1'-Spirobi(Indan)-5,5',6,6'-Tetrol Family. *J. Med. Chem.* **2000**, *43*, 2031–2039.

(91) Fritsch, D.; Bengtson, G.; Carta, M.; McKeown, N. B. Synthesis and Gas Permeation Properties of Spirobischromane-Based Polymers of Intrinsic Microporosity. *Macromol. Chem. Phys.* **2011**, *212*, 1137–1146.

(92) Rigaku Corporation. Crysalis Pro. Oxford, UK 2022.

(93) Sheldrick, G. M. SADABS. University of Göttingen, Germany 1996.

(94) Sheldrick, G. M. SHELXT – Integrated Space-Group and Crystal-Structure Determination. *Acta Crystallogr., Section A* **2015**, *71*, 3–8.

(95) Sheldrick, G. M. Crystal Structure Refinement with SHELXL. *Acta Crystallogr., Section C* **2015**, *71*, 3–8.

(96) Dolomanov, O. V.; Bourhis, L. J.; Gildea, R. J.; Howard, J. A. K. K.; Puschmann, H. OLEX2: A Complete Structure Solution, Refinement and Analysis Program. *J. Appl. Crystallogr.* **2009**, *42*, 339–341.

(97) van der Sluis, P.; Spek, A. L. BYPASS: An Effective Method for the Refinement of Crystal Structures Containing Disordered Solvent Regions. *Acta Crystallogr., Section A* **1990**, *46*, 194–201.

(98) Brahma, S.; Gardas, R. L. Understanding the Solvation Behavior of Pyrrolidinium Based Ionic Liquids in Acetonitrile through Thermophysical Properties at 293.15 to 328.15 K. *J. Mol. Liq.* **2018**, *256*, 22–28.

(99) Morgan, S. O.; Lowry, H. H. Dielectric Polarization of Some Pure Organic Compounds in the Dissolved, Liquid, and Solid States. *Journal of Physical Chemistry* **1930**, *34*, 2385–2432.

(100) Bain, G. A.; Berry, J. F. Diamagnetic Corrections and Pascal's Constants. *J. Chem. Educ.* **2008**, *85*, 532.

(101) Shoji, M.; Koizumi, K.; Kitagawa, Y.; Kawakami, T.; Yamanaka, S.; Okumura, M.; Yamaguchi, K. A General Algorithm for Calculation of Heisenberg Exchange Integrals J in Multispin Systems. *Chem Phys Lett* **2006**, *432*, 343–347.

(102) Chemcraft. 2013. *Graphical Software for Visualization ofQuantum Chemistry Computations*, https://www.chemcraftprog.com.

SYNOPSIS

The spin crossover behavior in a family of dinuclear Fe(III) complexes is modulated by the bridging bis(catecholate) ligand. Increasing the ligand field experienced by the Fe(III) ions stabilizes the mixed low spin-high spin state.